Università degli Studi di Ferrara

DOTTORATO DI RICERCA in FISICA

CICLO XXXVI

COORDINATRICE Prof.ssa Luppi Eleonora

Novel instrumentation for advanced Quantum Chromodynamics studies with flavor sensitivity

Settore Scientifico Disciplinare FIS/04

Dottorando

Dott. Vallarino Simone

Tutore

Prof. Contalbrigo Marco

ANNI 2020/2024

A Costy

i

Contents

Scientific motivation

The true nature of ordinary matter has always fascinated humankind, whose imagination has been pointed to the right direction since the 5th century BC with the first known atomic theory by Leucippus and Democritus. They described the matter as formed by small, invisible, indivisible, and eternal particles: the atoms. A long investigation followed them, including contributions from several of history's greatest philosophers and scientists. The progress led to the understanding that atoms have an internal structure consisting of a central nucleus composed of protons and neutrons, surrounded by a cloud of electrons. About 50 years ago, scientists discovered that nucleons also have an internal structure. Through the Deep Inelastic Scattering (DIS) experiments, on which a lepton is scattered off a nucleon, it was possible to access the distribution of partons inside the nucleon along the longitudinal direction defined by the hard-scale probe. It was a crucial step in developing Quantum Chromodynamics (QCD), currently the best theory describing the subatomic matter.

Ultimately, DIS was recognized as a limited tool to investigate the nucleon structure because it is mainly sensitive to observables at the probe's energy scale. In recent decades, theoretical developments have allowed defining soft-scale observables by measuring more complex processes. Reactions such as Semi-Inclusive Deep Inelastic Scattering (SIDIS) with single or di-hadron production, can provide information about the momentum of parton inside the nucleon. In particular, polarized SIDIS allows access to the Transverse-Momentum-Dependent (TMD) parton distributions describing the correlations of the quark and gluon degrees of freedom in transverse momentum and spin. This study can provide three-dimensional imaging of nucleon structure and inner dynamics, as long as the hadronic component in the final state can be measured. Identifying the species of the produced particles provides information on the quark flavor and assumes a crucial role in this context. The thesis describes the work carried out by the author in preparing novel instrumentation for particle identification in the final state of DIS experiments, to support modern analysis of the parton dynamics within the basic confined object (nucleon) with flavor sensitivity. The work has been focused on the CLAS12 spectrometer in operation at Jefferson Laboratory (JLab), Newport News, VA, USA, and the ePIC experiment in preparation for

the future Electron-Ion Collider (EIC) at Brookhaven National Laboratory (BNL), Long Island, NY, USA.

CLAS12 is a fixed-target experiment using a 12 GeV beam of polarized electrons scattering off polarized nuclear targets. In 2018 and 2022, two Ring Imaging Cherenkov (RICH) detector modules were installed to improve the $\pi^\pm/K^\pm$ separation in the high-momentum region (3÷8 GeV/c) of the experiment. The author contributed to the assembly, installation, and commissioning of the second RICH module, to the efficiency studies of the first module, and to the first SIDIS analysis with high-momentum kaons identified by the RICH. These studies led to the observation of the first spin asymmetry with high-momentum kaons from the CLAS12 experiment, and an initial assessment of the systematic error associated with the hadron identification.

ePIC will be the first experiment at the future EIC, the new collider designed to expand the frontiers of QCD. The author was involved in the development of the dual-radiator Ring Imaging Cherenkov (dRICH). This detector will interpolate the measurements of the Cherenkov angles of photons produced by relativistic particles crossing two different radiators to identify charged hadrons. The author contributed to the studies conducted with the dRICH prototype, developing the reconstruction and analysis software and simulations, characterizing the aerogel radiator samples, and being responsible for the tracking system used during the beam tests. The performance obtained by the prototype has been progressively improved and the results are now comparable with the expectation derived from the simulation and satisfy the requirements of the experiment.

In Chapter 1, the SIDIS theory is briefly introduced, outlying the connection with the experimental measurement. Chapter 2 includes the description of the CLAS12 RICH, its assembly and installation, and the efficiency study. In Chapter 3, the analysis of the Beam-Spin Asymmetry associated with SIDIS kaons is described. Chapter 4 describes the contribution to the dRICH for EIC, starting from a description of the ePIC experiment and focusing on the studies performed for the dRICH prototype. The conclusions of this work are summarized at the end.

Chapter 1

Investigate the non-perturbative QCD

This Chapter introduces non-perturbative Quantum Chromodynamics (QCD), outlining the importance of performing accurate measurements of polarized Semi-Inclusive Deep Inelastic Scattering (SIDIS) to understand the internal structure of the nucleon deeply. It describes how Beam-Spin Asymmetry (BSA) measurements permit access to the Transverse-Momentum-Dependent (TMD) distributions, encoding a three-dimensional imaging of nucleon structure and internal dynamics (in the momentum space). Finally, the instrumentation needed to perform this kind of measurement is introduced.

1.1 Introduction

Close to the mid-20th century, the invention of the cyclotron and synchrotron particle accelerators opened new possibilities for scientists to investigate the nature of nucleons. Simultaneously, the invention of the bubble chamber as the first modern detector allowed the so-called "particle explosion", meaning the discovery of many new particles in a few years. They include a lot of unstable particles and few stable states, all generically termed hadrons. This evidence suggested they are bound states of various elementary particles, and the unstable states had a decay channel, unlike the stable ones. While trying to classify them, both Gell-Mann[1] and Ne'eman[2] developed the eight-fold way [1, 2] of inserting the light hadrons and meson into multiples of flavor SU(3). Gell-Mann and Zweig[3] completed this idea by introducing the Quark Model (QM) [3, 4], which describes the mesons as bound states of quark

---

[1]Murray Gell-Mann, September 15, 1929, Manhattan, New York City, U.S. - May 24, 2019, Santa Fe, New Mexico, U.S.; Winner of 1969 Nobel Prize in Physics.

[2]Yuval Ne'eman, 14 May 1925, Tel Aviv, Mandatory Palestine - 26 April 2006 Tel Aviv, Israel.

[3]George Zweig, May 20, 1937, Moscow, Russian SFSR, Soviet Union.

1
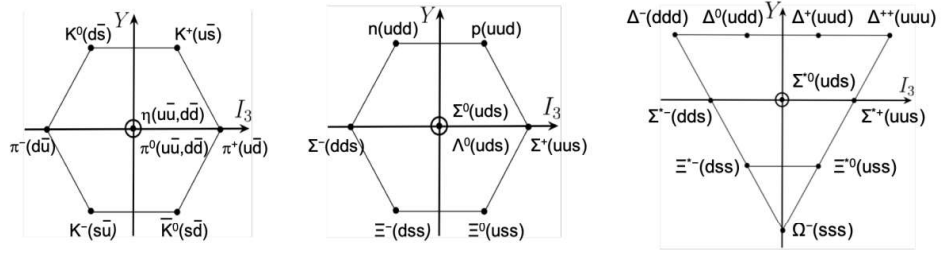
Figure 1.1: Representation of the Quark Model, taken from Reference [5].

and anti-quark pair and the baryons as bound states of three quarks with different flavors *up*, *down*, and *strange* (u,d,s) as represented in Figure 1.1.

The QM was initially treated as a mathematical trick permitting the description of several particles, but the existence of elementary components of hadrons with spin-$\frac{1}{2}$ and fractional charge was not accepted as realistic. Moreover, the original version showed issues with not-trivial solutions, for example, the $\Delta^{++}(1232)$ baryon: it was a bound state of three up quarks *uuu*. It was a fermion described by a forbidden wave function that was symmetric under the exchange of any two quarks, assuming that the elementary particles were in the fundamental state described by a S-wave. Introducing a new quantum number called *color* permitted the solution to this issue [6]. Indeed, assuming three possible color states, i.e. the fundamental color *red*, *green*, and *blue*, the Δ^{++} wave functions became antisymmetric under the exchange of two quarks with different colors, as required for fermions. In 1964, this was the first step into Quantum Chromodynamics (QCD), the most modern theory describing the nucleon structure [5, 7]. A side effect of introducing the color quantum number was the expectation of eight colored statuses for each meson that were not observed. Moreover, it turned out to be completely impossible to isolate and detect individual quarks, requiring the addition of other constraints in the theory. The continuous necessity of introducing new hypotheses to solve the underlying issues caused widespread skepticism toward the theory.

In the 1960s, there was a breakthrough due to the Deep Inelastic Scattering (DIS) experiments performed by Friedman[4], Kendall[5], and Taylor[6] at Stanford Linear Accelerator Center (SLAC) and Massachusetts Institute of Technology (MIT)[8–10]. They confirmed the nucleon contains point-like spin-$\frac{1}{2}$ particles, providing the first experimental measurement of the quark's

---

[4]Jerome Isaac Friedman, March 28, 1930, Chicago, Illinois, U.S.; Bio, Winner of the 1990 Nobel Prize in Physics

[5]Henry Way Kendall, December 9, 1926, Boston, Massachusetts, U.S - February 15, 1999, Wakulla Springs State Park, Florida, U.S.; Winner of the 1990 Nobel Prize in Physics

[6]Richard Edward Taylor, 2 November 1929, Medicine Hat, Alberta, Canada - 22 February 2018, Stanford, California, U.S.; Winner of 1990 Nobel Prize in Physics

existence. The interpretation of their results by Bjorken[7] and Feynman[8] led to the so-called Parton Model (PM), the first step toward a more precise description of hadrons [11–13].

The DIS is the scattering of lepton l off a nucleon N, where the scattered lepton is detected

$$\ell(l) + N(P) \rightarrow \ell(l') + X \qquad (1.1)$$

and the quantities in parenthesis are the particles' momentum. A sketch of DIS is shown in Figure 1.2a. By measuring the scattered lepton, the four-momentum transferred from the probe in the collision can be defined as

$$q = l - l' \qquad (1.2)$$

where l and l' are the four-momentum of the incident and scattered lepton, and the transferred invariant momentum as

$$Q = \sqrt{-q^2}. \qquad (1.3)$$

Q defines the nominal wavelength of the probe and the spatial scale L that can be resolved experimentally

$$Q = \frac{\hbar}{L} \qquad (1.4)$$

thus it can be taken to identify the scale of the interaction. In the following, the natural unit system $\hbar = c = 1$ is used.

If $Q \gg \frac{1}{R}$, where R is the proton radius, the Deep Inelastic Scattering (DIS) can be described as the short-range interaction of the electron with a point-like constituent of the nucleon. Feynman called these point-like spin-$\frac{1}{2}$ objects *partons*, the basic building of the Parton Model (PM). In this model, Feynman describes the DIS cross-section in the infinite momentum frame, where partons are moving in a collinear way, bringing a fraction x of the total nucleon momentum, with the formula

$$E' \frac{d\sigma_{ep \rightarrow e'X}}{d^3 l'} \approx \sum_i e_i^2 \left\{ \frac{2\alpha^2}{Q^2(\ell + P)^2} \left[\frac{1 + (1 - y)^2}{y} \right] \right\} f_{i/p}(x) \qquad (1.5)$$

where the sum is over all the possible types of partons, e_i is the charge of the parton, α is the electromagnetic fine constant, P is the four-momentum of the target, $y = \frac{P \cdot q}{P \cdot \ell}$ is the fraction of energy loss by the lepton, and $x = x_B = \frac{Q^2}{2P \cdot q}$ is the Bjorken variable representing the fraction of the proton momentum carried by the parton. The most interesting term is the function $f_{i/p}(x)$, which represents the probability of finding a type i parton

---

[7]James Daniel "BJ" Bjorken, June 22, 1934, Chicago, Illinois, United States

[8]Richard Phillips Feynman, May 11, 1918, New York City, U.S. - February 15, 1988, Los Angeles, California, U.S.; Winner of the 1964 Nobel Prize in Physics
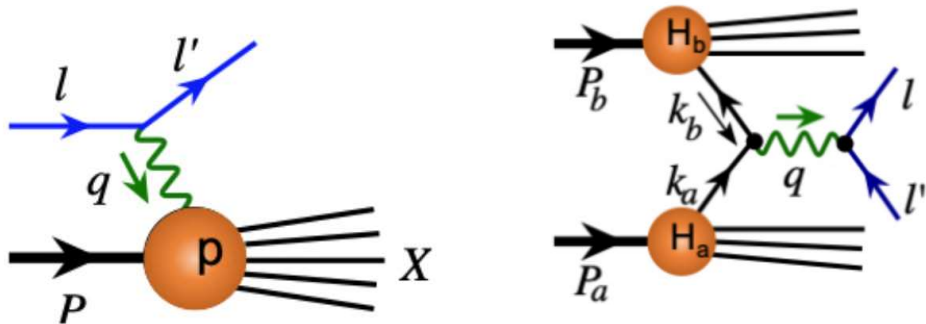
(a) Diagram of the Deep Inelastic Scattering.

(b) Diagram of the DY process.

Figure 1.2: Sketches were taken from Reference [5]

carrying a fraction x of the proton momentum. In the PM, $f_{i/p}(x)$ takes the name of Parton Distribution Function (PDF). From this formula, it is possible to show that the DIS cross-section is independent of the transferred momentum but depends only on x_B, a phenomenon known as Bjorken scaling and experimentally verified at SLAC. These measurements provided the first credibility to the quark idea, pushing forward in the direction of theorizing the Quark Parton Model (QPM), where the partons are identified as the quarks. The quarks are described as spin-$\frac{1}{2}$ particles with a fractional electrical charge of $+\frac{2}{3}$ for the *up*, and $-\frac{1}{3}$ for *down* and *strange* quark, and with three possible color charges *red*, *green*, and *blue*.

An independent confirmation of the QPM became from the so-called Drell-Yan (DY) process [14], the production of a lepton pair from the scattering of two hadrons:

$$H_a + H_b \rightarrow l + \bar{l} \tag{1.6}$$

By describing it as the annihilation of a quark and anti-quark, it was possible to compute the expectation value of the cross-section using the PDFs obtained by the DIS measurements. Except for a kinematic factor ~ 2, the theoretical and experimental cross-sections were found to be the same [15].

The QPM was a significant step toward the understanding of the nucleon's inner structure, but a new and more general gauge theory was soon after developed: the Quantum Chromodynamics (QCD), where the quarks are held together by the gluons, the boson mediating the strong color force. In QCD, the nucleon is described as a relativistic bound state of quarks and gluons, collectively referred to as partons. Despite more than fifty years of studies, there are still outstanding questions in QCD. Two of the most surprising effects of the QCD are the *color confinement*, which implies that a struck quark in the scattering process does generate new particles to obtain a colorless final state, and the *asymptotic freedom*, which made the strong force weakly coupled at a sufficiently short distance. The former automatically

explains the observed impossibility of isolating the partons, causing the so-called process of "hadronization" on which a struck quark, ejected from the nucleon, generates other quarks and anti-quarks, to form a new colorless hadron. The latter makes it possible the QCD factorization, a theoretical formalism that permits linking the quark and gluon information to the final state particles measured by modern high-energy physics experiments. In this formalism, the reactions can be described by a well-defined set of PDFs encoding information on nucleon's structure, and Fragmentation Functions (FFs) describing the parton hadronization. These functions can not yet been calculated from first principles in QCD, but they are universal (valid in any reaction) and their evolution with the scale Q has been described by the DGLAP formalism. The precise determination of these distributions from experimental data permits to explore the quarks' and gluons' dynamics, and access the nucleon structure, even without effectively "seeing" the quarks.

QCD is a quantum field theory [16, 17], and its Lagrange density is built on two kinds of particle fields: the spin-$\frac{1}{2}$ Dirac fields ψ_f^i and the massless spin-1 vector field A_μ^a. The former field is associated with the quarks, i can assume the value of the three colors *red, green,* and *blue,* and f labels the six flavors of quarks *up, down, strange, charm, bottom,* and *top.* The latter field is associated with the gluons, a can assume eight possible values corresponding to the square of the number of colors minus one. Having a SU(3) symmetry, the Lagrange density is:

$$\mathcal{L}_{QCD}(\psi_f, A_\mu) = -\frac{1}{4}G_{\mu\nu,a}^2[A] + \sum_f \overline{\psi}_f \left(iD_\mu[A]\gamma^\mu - m_f\right)\psi_f \qquad (1.7)$$

where the gluon field strength $G_{\mu\nu,a}[A]$ and the covariant derivative $D_\mu[A]$ contain the strong coupling constant, and the generator and structure constant defining the SU(3) color algebra. The QCD is a renormalizable theory, and it is characterized by a running coupling $\alpha(\mu)$ depending on the energy scale at which the interaction is probed. Differently from the electromagnetic interaction, the $\alpha(\mu)$ decreases for increasing μ, i.e. the strong interaction became weaker at a short distance or high transferred momentum. This property is closely linked to the asymptotic freedom, making it possible to use the perturbation theory to describe the QCD dynamics at short distances.

The strong interactions at the scale of confinement occur at $\Lambda_{\mathrm{QCD}} \sim 200\,\mathrm{MeV}$, making the coupling constant so large that the perturbation theory is not applicable. It means the scattering cross-section involving hadrons can not be computed using only the perturbative QCD. The information of non-perturbative components of the hadron is embedded inside the PDFs, while QCD factorization enables the systematic separation of physical phenomena occurring at distinct momentum scales. In particular, the nucleon's internal structure can be described by the matrix elements of gauge-invariant partonic operators composed of quark and gluon fields with different spin projections.

These matrix elements are not observables, as could be expected for the color confinement, but the QCD factorization links them to measurable cross-sections.

Probing via scattering the spin-$\frac{1}{2}$ quark carrying the momentum fraction x, three possible polarization states can be studied: unpolarized, longitudinally polarized, and transversely polarized. Considering a spin-$\frac{1}{2}$ nucleon, three leading order collinear PDFs can be defined: the *unpolarized* collinear distribution $f_{q/h}(x)$, a quark q inside an unpolarized nucleon, the collinear *helicity* distribution $\Delta f_{q/h}(x)$ of a longitudinally polarized quark q inside a longitudinally polarized nucleon, and the collinear *transversity* distribution $\delta f_{q/h}(x)^9$ of a transversely polarized quark q inside a transversely polarized nucleon (with the direction of quark transverse polarization parallel to the direction of nucleon's polarization). The first is well-determined from existing experimental data, while precise measurements of the others are expected from the experiments at JLab [18, 19] and EIC [20].

A high Q is needed to allow the probe to localize the parton. Scattering with high transferred momentum $Q \gg \frac{1}{R}$ is not sensitive to the genuine physics at the scale $\Lambda_{QCD} \sim \frac{1}{R}$, including the parton confined transverse motion in the momentum space and its spatial distribution in position space. On the other hand, a secondary soft momentum scale $Q_2 \ll Q_1$ is needed to access dimensions other than the collinear momentum fraction. Two different scales remain a manageable problem for the QCD factorization. For example, the DY cross-section is a two-scale observable: when studied as a function of the pair's transverse momentum module $q_T = |\mathbf{q}_T|$, in addition to the invariant mass of the lepton pair Q. The momentum $\mathbf{q}_T$ constituted by the sum of the transverse momentum components of the quark and anti-quark annihilated pair, provides direct access to the transverse momentum of the quarks. The cross-section formula, in this case, depends on $f_1(x_a, \mathbf{k}_{aT})$, a Transverse-Momentum-Dependent (TMD) associated with the parton. Accessing the two different scales allows us to define a class of functions called TMD distributions, similar to the PDFs, but providing the probability density of finding a parton carrying a fraction of the longitudinal momentum x and transverse momentum $\mathbf{k}_T$ inside the nucleon. They are also identified as TMD PDFs. As a consequence, TMD distributions provide more information on the three-dimensional hadron structure than the simple collinear PDFs because can take into account complex correlations with, e.g., spin. The TMD distributions are classified in terms of the correlation between spins' polarizations, detecting asymmetries of cross-sections with polarized beams and targets can provide multiple independent observables. Some TMD PDFs, like $f(x, \mathbf{k}_T)$, $\delta_q(x, \mathbf{k}_T)$, and $h(x, \mathbf{k}_T)$ are natural extensions of the parton distributions and fragmentation functions defined above in the three-dimensional momentum space. However, there are also TMD distributions not having a corresponding

---

[9] In literature, it is also written as $h_1(x)$ or $\delta q(x)$

6

Figure 1.3: Recap of the Transverse-Momentum-Dependent parton distributions as a function of nucleon and quark polarization. The table is taken from Reference [5].

mono-dimensional PDF, i.e., they vanish whenever integrated in transverse momentum. For example, the *Sivers function* $f_{1T}^{\perp}(x, \mathbf{k}_T)$ represents the correlation between the direction of the transverse spin of the nucleon and the direction of transverse motion of an unpolarized active quark, as well as its flavor dependence. It encodes the correlation between the partonic intrinsic motion and the transverse spin of the nucleon, and it generates a dipole deformation in momentum space that could not exist without the contribution of the orbital angular momentum of partons. Several groups extracted the Sivers function from SIDIS data with consistent results [21–30], demonstrating the existence of non-zero contribution of the parton angular momentum to the nucleon spin. Another example of non-vanishing TMD is the *pretzelosity* $h_{1T}^{\perp}(x, \mathbf{k}_T)$ representing how the nucleon spin and quark spin correlation can influence the quark's transverse motion.

TMD distributions are classified using the twist, a quantity that describes the scaling behavior with respect to the transferred momentum Q. The most important TMD distributions are twist-two, also called leading-twist or leading-power, and twist-three TMD distributions, also called subleading. Considering nucleon' and quark' spin polarization, eight TMD distributions can be defined at leading-order (twist). A scheme linking the TMD with the spins polarization is shown in Figure 1.3. Similar TMD distributions exist for anti-quark and gluon.
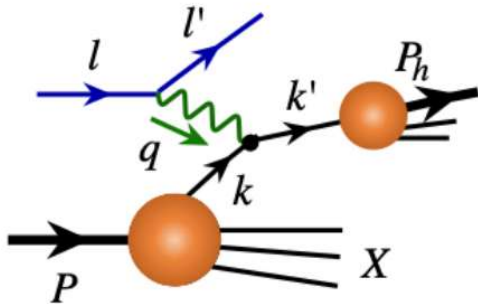
Figure 1.4: Scheme of the Semi-Inclusive Deep Inelastic Scattering (SIDIS), image taken from Reference [5].

1.2 Measuring the Transverse-Momentum-Dependent parton distribution

The existence of a QCD factorization implies the possibility of accessing the three-dimensional nucleon structure via the TMD distributions measurement, relating them to physical observables, as described before for the DY process. Indeed, the QCD factorization, DY process is described as the product of quark and anti-quark TMD PDFs, not allowing the disentanglement of the single quarks or gluon contribution or accesses gluons distributions. A different process to accessing the TMD distributions is the back-to-back dihadron in e^+e^- collisions, which is described as the product of TMD FFs, with no information on the distribution of quark inside the nucleon

$$e^+ + e^- \to H_1(P_1) + H_2(P_2) + X. \tag{1.8}$$

When the hadrons are almost back-to-back the momentum imbalance $\bar{p} = |\vec{P}_1 + \vec{P}_2| \ll \frac{|\vec{P}_1 - \vec{P}_2|}{2} = \overline{P}$ defines a soft-scale in addition to the hard scale of the invariant mass of the pair, providing a second possible channel to investigate the quark fragmentation.

There is another factorizable two-scale observable, which is described as a product of TMD PDFs and FFs: the polarized Semi-Inclusive Deep Inelastic Scattering (SIDIS). It provides access to the nucleon structure and its internal dynamics but is diluted in the hadronization process. In polarized Semi-Inclusive Deep Inelastic Scattering (SIDIS) a polarized lepton ℓ hits a polarized nucleon target N and produces a final state including the scattered lepton and at least one measured hadron H

$$\ell + N \to \ell + H + X. \tag{1.9}$$

The process can be described by the scheme shown in Figure 1.4. In this case, the hard scale is the transferred momentum $Q \gg \Lambda_{QCD}$, and the soft scale

Figure 1.5: Recap of the Transverse-Momentum-Dependent Fragmentation Functions as a function of nucleon and quark polarization. Table taken from Reference [5]

is the transverse momentum of the hadron observed in the final state $p_{H,T}$. SIDIS is a powerful two-scale observable giving access to the three-dimensional structure of the nucleon. To write the SIDIS cross-section including TMD distributions, it is necessary to introduce a new kind of distribution depending on the quark transverse momentum, the TMD Fragmentation Functions (FFs) $D_{h/q}(\zeta, \mathbf{k'}_T)$. They represent the probability of a quark q to hadronize in the hadron h carrying the momentum fraction ζ of the fragmenting quark momentum and with transverse momentum $\mathbf{k'}_T$ with respect the originating quark direction. Usually, the acronym TMDs includes both the TMD PDFs, describing the probability of finding a quark with a certain momentum inside the hadron, and the TMD FFs. As for TMD PDFs, it is possible to define eight leading-order TMD FFs for the quark, that are reported in Figure 1.5, as well it is possible to define analogous TMD FFs for anti-quark and gluon.

In SIDIS, observing the target from the point of view of the probe, it does not look spherical but rather like a flat disk due to the Lorentz contraction. Many questions about TMDs are currently unanswered; for example, it is unclear if the parton density in momentum space is higher in the disk's center and decreases monotonically to the edge or vice-versa. The distributions change depending on the energy scale of the probe and on the value of the longitudinal fractional momentum. It is also unknown if there is a difference in
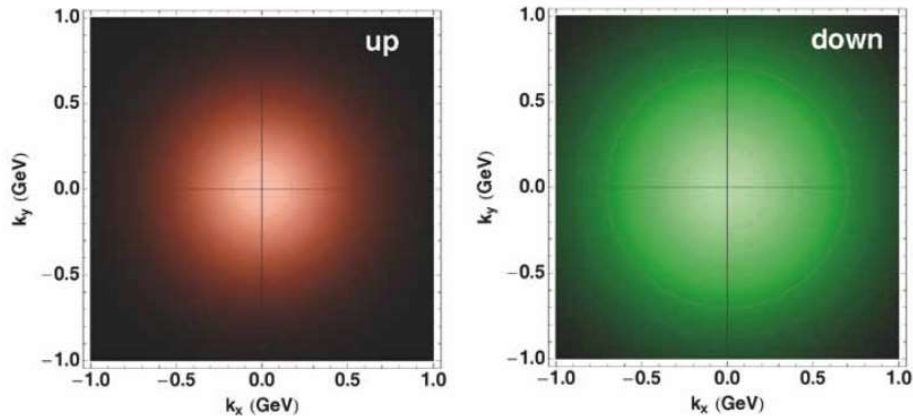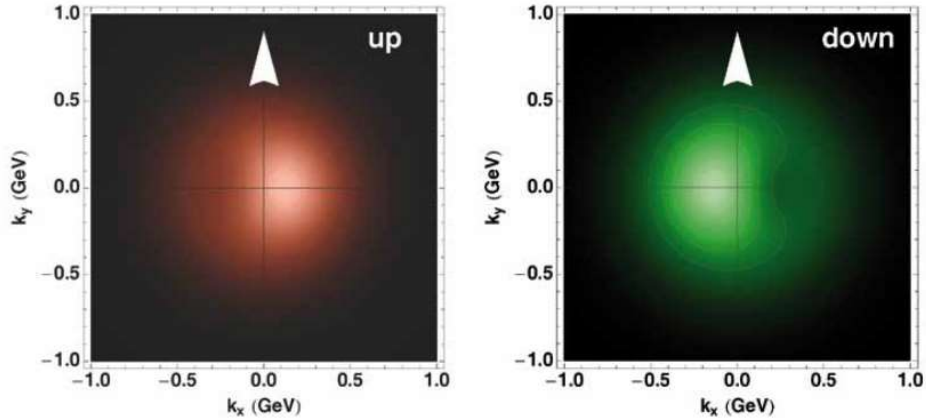
Figure 1.6: Distribution of up and down-quark transverse momentum. The down-quark distribution is larger than the top-quark. Image taken from Reference [31]

the distribution of partons with different flavors. For example, it is unknown if one flavor is more concentrated in the center and the other on the sides, or if the flavors are uniformly mixed. There are just first indications that the up-quark distribution is closer to the center of the nucleon than the down-quark distribution, as shown in Figure 1.6.

The introduction of a preferred nucleon's spin direction (polarization) causes even more strange effects. Suppose the nucleon is moving toward us, and its spin is pointing upwards: it turns out that the up-quarks move preferentially to the right and down-quarks to the left, as shown in Figure 1.7. These distributions are not anymore cylindrical symmetric in the momentum space and signal not trivial inner dynamic correlations.

The first measurements on TMD distributions were performed in the early 2000s, from experiments like HERMES at Deutsches Elektronen-Synchrotron (DESY), COMPASS at European Council for Nuclear Research (CERN), and various experiments at Jefferson Laboratory (JLab). HERMES exploited the scattering of the 27.5 GeV beam of polarized electrons provided by the Hadron-Elektron-Ringanlage (HERA) accelerator off an internal target of gas, taking data in two runs between 1995 and 2007. COMPASS was a fixed target experiment in the CERN north area. It acquired data from 2001 till 2021 using the high-energy ($100 \div 200$ GeV) muons of the SPS secondary beam. The JLab experiments exploited the scattering of 6 GeV CEBAF polarized electrons beam of fixed nuclear targets, acquiring data from 1995 to 2008. These measurements led to the previously mentioned results, generating impetus for further study of the structure of subatomic matter. Indeed, the physics programs of existing or future experimental facilities indicate polarized SIDIS and DY processes as the main tools to

Figure 1.7: Distribution of up and down-quark transverse momentum, if the nucleon spin is pointing upward and the nucleon comes out of the paper. Image taken from Reference [31]

expand the QCD frontiers. Among these facilities are the running CEBAF after the 12 GeV upgrade at Jefferson Laboratory [18], and the RHIC [32] at Brookhaven National Laboratory (BNL), the LHC fixed-target experiment (LHCspin) [33] at CERN, and the future Electron-Ion Collider (EIC) [20] at BNL. Reference [34] contains a recap of the most recent results in polarized SIDIS.

1.3 Polarized Semi-Inclusive Deep Inelastic Scattering

The polarized SIDIS on which a polarized lepton ℓ hits a polarized nucleon target N and produces a final state including the scattered lepton and at least one measured hadron h

$$\ell(l) + N(P) \rightarrow \ell(l') + h(P_h) + X \tag{1.10}$$

where the quantities in parentheses represent the four-momenta. The kinematic of the reaction is described in figure 1.8. In the limit of $Q \ll m_{W,Z}$ the interaction can be described as a single photon exchange, then the

11
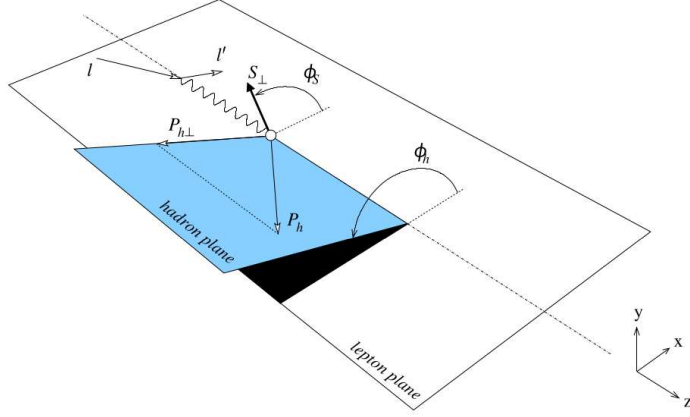
Figure 1.8: Definition of azimuthal angles for SIDIS

cross-section can be expressed [35] as:

$$
\frac{d\sigma}{dx_B \ dy \ d\psi \ dz \ d\phi_h \ dP_{h\perp}^2} =
$$

$$
\frac{\alpha^2}{x\,y\,Q^2}\frac{y^2}{2\,(1-\varepsilon)}\left(1+\frac{\gamma^2}{2x_B}\right)\Bigg\{ F_{UU,T} + \varepsilon F_{UU,L} + \sqrt{2\varepsilon(1+\varepsilon)}\cos\phi_h F_{UU}^{\cos\phi_h} +
$$

$$
+\,\varepsilon\cos(2\phi_h)F_{UU}^{\cos 2\phi_h} + \lambda_e\sqrt{2\varepsilon(1-\varepsilon)}\sin\phi_h F_{LU}^{\sin\phi_h} +
$$

$$
+\,S_\parallel\left[\sqrt{2\varepsilon(1+\varepsilon)}\sin\phi_h F_{UL}^{\sin\phi_h} + \varepsilon\sin 2\phi_h F_{UL}^{\sin\phi_h}\right] +
$$

$$
+\,S_\parallel\lambda_e\left[\sqrt{1-\varepsilon^2}F_{LL} + \sqrt{2\varepsilon(1-\varepsilon)}\cos\phi_h F_{LL}^{\cos\phi_h}\right] +
$$

$$
+\,|\mathbf{S}_\perp|\left[\sin\left(\phi_h-\phi_S\right)\left(F_{UT,T}^{\sin(\phi_h-\phi_S)} + \varepsilon F_{UT,L}^{\sin\phi_h-\phi_S}\right) +
$$

$$
+\,\varepsilon\sin(\phi_h+\phi_S)F_{UT}^{\sin(\phi_h+\phi_S)} + \varepsilon\sin\left(3\phi_h-\phi_S\right)F_{UT}^{\sin(3\phi_h-\phi_S)}
$$

$$
+\,\sqrt{2\varepsilon(1+\varepsilon)}\sin\phi_S F_{UT}^{\sin\phi_S} + \sqrt{2\varepsilon(1+\varepsilon)}\sin\left(2\phi_h-\phi_S\right)F_{UT}^{\sin(2\phi_h-\phi_S)}\right] +
$$

$$
+\,|\mathbf{S}_\perp|\lambda_e\left[\sqrt{1-\varepsilon^2}\cos\left(\phi_h-\phi_S\right)F_{LT}^{\cos(\phi_h-\phi_S)} + \sqrt{2\varepsilon(1-\varepsilon)}\cos\phi_S F_{LT}^{\cos\phi_S} +
$$

$$
\sqrt{2\varepsilon(1-\varepsilon)}\cos\left(2\phi_h-\phi_S\right)F_{LT}^{\cos(2\phi_h-\phi_S)}\right]\Bigg\} \tag{1.11}
$$

where α is the fine structure constant, and the $F_{XY,Z}^{weight}$ are the structure functions connecting the cross-section with the TMD distributions. The apex *weight* represents the modulation associated with each structure function, which depends on the angles ϕ_h and ϕ_S. The first and second subscripts on the structure functions indicate the polarization *Longitudinal, Transverse,* or *Unpolarized* of the beam and the target. The third subscript, if present,

indicates the polarization of the virtual photon. The quantities $S_{\parallel}$ and $S_{\perp}$ are the components of the target spin vector, ϕ_h is the azimuthal angle of the outgoing hadron, ϕ_S the angle defined by the target spin vector S all referred to the lepton scattering plane. The quantity ε is the ratio between the longitudinal and transverse photon flux

$$\varepsilon = \frac{1 - y - \frac{\gamma^2 y^2}{4}}{1 - y + \frac{y^2}{2} + \frac{\gamma^2 y^2}{4}} \tag{1.12}$$

where y is the usual variable of the DIS

$$y = \frac{P \cdot q}{P \cdot l} \tag{1.13}$$

and P is the 4-momentum of the target nucleon, q the virtual photon one, and l the beam lepton one.

The structure functions F_{XY}^{weight} can be seen as the coefficients of the Fourier expansion of the SIDIS cross-section, and can be expressed in the form of a combination of TMDs. The specific expression of each structure function can be derived following considerations on the quark-quark and quark-gluon-quark correlation functions, which can be considered as the equation-of-motion for QCD. They provide constraints on which TMD distributions contribute to a specific structure-function. For example, the UU structure-functions are expressed by

$$F_{UU,T} = \mathcal{C}\left[f_1 D_1\right] \tag{1.14}$$

$$F_{UU,L} = 0 \tag{1.15}$$

$$F_{UU}^{\cos\phi} = \frac{2M}{Q}\mathcal{C}\left[-\frac{\hat{\mathbf{h}} \cdot \mathbf{k}_T}{M_H}\left(x_B h H_1^{\perp} + \frac{M_h}{M}f_1\frac{\tilde{D}^{\perp}}{z}\right)\right.$$
$$\left. -\frac{\hat{\mathbf{h}} \cdot \mathbf{p}_T}{M}\left(x_B f^{\perp}D_1 + \frac{M_h}{M}h_1^{\perp}\frac{\tilde{H}}{z}\right)\right] \tag{1.16}$$

$$F_{UU}^{\cos 2\phi_h} = \mathcal{C}\left[-\frac{2\left(\hat{\mathbf{h}} \cdot \mathbf{k}_T\right)\left(\hat{\mathbf{h}} \cdot \mathbf{p}_T\right) - (\mathbf{k}_T \cdot \mathbf{p}_T)}{MM_H}h_1^{\perp}H_1^{\perp}\right]. \tag{1.17}$$

In the above expressions always appear a convolution between a TMD PDF and a TMD FF. For example

$$\mathcal{C}[wfD] = x\sum_a e_a^2 \int d^2\mathbf{p}_T d^2\mathbf{k}_T \delta^{(2)}(\mathbf{p}_T - \mathbf{k}_T - \frac{\mathbf{P}_{h\perp}}{z})w(\mathbf{p}_T, \mathbf{k}_T)f^a(x, p_T^2)D^a(z, k_T^2) \tag{1.18}$$

where f_a is the unpolarized TMD PDF and D_a is the unpolarized TMD FF, the summation runs over quarks and antiquarks, $\mathbf{p}_T$ and $\mathbf{k}_T$ are the intrinsic

quark transverse momentum in the target and generated in hadronization respectively, w is a calculable kinematic term with

$$\hat{\mathbf{h}} = \mathbf{P}_{h\perp}/|\mathbf{P}_{h\perp}|. \tag{1.19}$$

As anticipated, the equations recall the feature of SIDIS to be described by the product of TMD PDFs and FFs. A complete discussion can be found in Reference [35]. Many structure functions can be associated with spin asymmetries, which means there is an asymmetry depending on the angle ϕ_h and ϕ_s between the number of events obtained with different beam and target polarizations. The measurement of experimental asymmetries allows us to access the structure functions and then extract the TMDs although complex calculations are necessary to solve the convolution.

1.4 Beam-Spin Asymmetry

An interesting possibility is to measure the Beam-Spin Asymmetry (BSA), the asymmetry related to the longitudinal polarization of the beam, which will be used as a case study. The BSA can be expressed as

$$A_{LU} = \frac{d\sigma^+ - d\sigma^-}{d\sigma^+ + d\sigma^-} = \frac{A_{LU}^{\sin\phi^h}\sin\phi^h}{1 + A_{UU}^{\cos\phi^h}\cos\phi^h + A_{UU}^{\cos 2\phi^h}\cos 2\phi^h} \tag{1.20}$$

where $d\sigma^\pm$ is the differential cross-section for each beam helicity state (parallel or antiparallel), and $A_{LU}^{\sin\phi^h}$, $A_{UU}^{\cos\phi^h}$, $A_{UU}^{\cos 2\phi^h}$ are the asymmetry terms, which are related to the structure functions. The angle ϕ^h will be usually indicated as ϕ in the following. From the measurement of $A_{LU}^{\sin\phi}$ it is possible to obtain the correspondent structure function via

$$A_{LU}^{\sin\phi} = \frac{\sqrt{2\varepsilon(1-\varepsilon)}F_{LU}^{\sin\phi}}{F_{UU}} \tag{1.21}$$

where $F_{UU} = F_{UU,T} + \varepsilon F_{UU,L}$ and ε is defined in Equation 1.12. Starting from an asymmetry, the structure functions of interest are usually derived as a ratio with the unpolarized one.

Experimentally, the BSA is defined as

$$A_{LU}(\phi) = \frac{1}{P_b}\frac{N^+ - N^-}{N^+ + N^-} \tag{1.22}$$

where P_b is the beam polarization and $N^\pm$ the number of events with positive or negative beam helicity.

The cross-section term $F_{LU}^{\sin\phi}$ is related to the TMD distributions by the following expression

$$F_{LU}^{\sin\phi} = \frac{2M}{Q}\mathcal{C}\left[\frac{\hat{\mathbf{h}}\cdot\mathbf{k}_T}{M_H}\left(x_B e H_1^{\perp} + \frac{M_h}{M}f_1\frac{\tilde{G}^{\perp}}{z}\right)\right.$$
$$\left.+\frac{\hat{\mathbf{h}}\cdot\mathbf{p}_T}{M}\left(x_B g^{\perp}D_1 + \frac{M_h}{M}h_1^{\perp}\frac{\tilde{E}}{z}\right)\right] \tag{1.23}$$

where M and M_h are the mass of the target and hadron, Q^2 the transferred momentum, $\mathbf{p}_T$ and $\mathbf{k}_T$ are the intrinsic quark transverse momentum in the target and fragmentation, respectively. The TMD function $h_1^{\perp}$ is the leading-twist Boer-Mulders PDF, $H_1^{\perp}$ is the leading-twist Collins FF, f_1 is the unpolarized PDF, D_1 is the unpolarized FF, e and $g^{\perp}$ are twist-3 PDFs, and $\tilde{G}^{\perp}$ and $\tilde{E}$ are twist-3 FFs.

Most of the twist-three structure functions can be separated into three terms using QCD's equation of motions: a twist-two piece, related to a single-parton density, a genuine twist-three term containing information on quark-gluon correlation and dynamical chiral symmetry breaking, and a term proportional to the current-quark mass, which is usually neglected for light quarks [36]. The $F_{LU}^{\sin\phi}$ is particularly interesting. In the Wandzura-Wilczek approximation [37], it is expected the related asymmetry becomes zero because of the vanishing of the twist-two terms. This expectation is contradicted by the existing measurement of the asymmetry in the order of $\sim 2\%$. Then $F_{LU}^{\sin\phi}$ is a twist-three structure-function, particularly sensitive to the quark-gluon correlation. In the case of CLAS12, it can be reliably measured thanks to the high polarization of the electron beam.

1.5 This work

TMD distributions represent a revolution in the classical approach investigating the internal structure of nucleons and scattering processes. They opened a new window for exploring the details of the nucleon structure and inner dynamics. However, their complete characterization through SIDIS requires an excellent PID system, capable of discriminating between different particles to provide adequate flavor sensitivity. To access the different flavor partons is crucial for unraveling the complex interactions within the confined nucleons state and advancing in our understanding of QCD.

Recently, the CLAS collaboration, which runs the CLAS12 spectrometer at JLab, published a first high-precision measurement of $F_{LU}^{\sin\phi}$ for the π^+ SIDIS [38]. An analogous result for kaon SIDIS was not immediate to obtain because the original Particle Identification (PID) system was designed for the pion/electron separation with the 6 GeV beam, so it did not have the capability to distinguish the high-momentum charged pion and kaon. With

the energy upgrade, it was decided to introduce a new component into the baseline spectrometer to improve the PID, despite CLAS12 was already under construction. Two modules of Ring Imaging Cherenkov (RICH) detector were installed at CLAS12 in 2018 and 2022, extending the capability of high momentum particle identification. The detector features an innovative hybrid-optics design, that was developed to fit in the limited available space and minimize the cost and the material budget. The author was significantly involved in the assembly and commissioning of the second module and in the efficiency study of the first module. Moreover, he performed a preliminary measurement of $F_{LU}^{\sin\phi}$ for kaons evaluating the impact of the RICH. These activities are described in the Chapters 2 and 3.

The JLab management and user community are evaluating the possibility of a new energy and luminosity upgrade [39]. It will bring the beam energy above $20\,\mathrm{GeV}$ and at least double the luminosity, with the option to increase it by one order of magnitude. The Figures 1.9a and 1.9b show the phase space that will be covered after the upgrade. The high precision measurements possible at JLab complement the ones at the Electron-Ion Collider (EIC), the powerful new high-luminosity collider of polarized beams that will be located at Brookhaven National Laboratory. In the next decades, new breakthrough measurements will probably come from EIC, designed to be a large-scale facility for three-dimensional nucleon imaging. For SIDIS at EIC, particle identification in the hadronic endcap will play a crucial role, facing several technical challenges like identifying particles in a broad momentum range, working in a high-magnetic field and curing radiation damage of solid-state photosensors in situ. The author significantly contributed to the design of the dual-radiator Ring Imaging Cherenkov (dRICH), in particular, performing the studies on the prototype developed and operated by a collaboration led by INFN Ferrara between 2021 and 2023. The activities regarding the dRICH are described in Chapter 4.

Working on these two experimental lines, the author has contributed to the development of novel instrumentation for the study of QCD with a modern approach (TMDs) and flavor sensitivity.
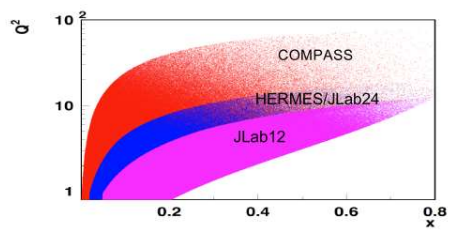
(a) The phase space covered by the JLab experiments after the first energy upgrade. It is complementary with the COMPASS and HERMES.
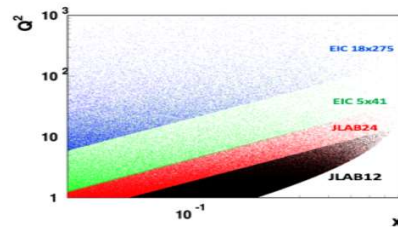
(b) The phase space that will be covered by the JLab experiments after the new energy upgrade. It will allow access to the complementary region of the new Electron-Ion Collider.

Figure 1.9

Chapter 2

The Ring Imaging Cherenkov detector for CLAS12

To perform QCD measurements with flavor sensitivity, an efficient system to identify the hadrons in the final state is essential. This Chapter introduces the CLAS12 spectrometer focusing on the PID system and describes the Ring Imaging Cherenkov (RICH) detector. During this work, the author was involved in the assembly and commissioning of the second RICH module, in the efficiency study of the first module, and in the first physics analysis carried out using the RICH data. The first two of these activities are described in this Chapter.

2.1 The CLAS12 spectrometer at Jefferson Lab

The Thomas Jefferson National Accelerator Facility (JLab) is one of the most important laboratories dedicated to nuclear physics research thanks to the electron beam provided by the Continuous Electron Beams Accelerator Facility (CEBAF) and different apparatuses realized in four experimental halls. The JLab site is shown in Figure 2.1. The high intensity, highly polarized, 12 GeV electron beam permits to perform sophisticated measurements aiming to probe and possibly extend the Standard Model of particle physics via precise parity violation measurement, light dark matter and exotic particle searches, three-dimensional nucleon structure and parton dynamics investigation, exploiting the peculiarities of the four halls. A scheme of CEBAF is represented in Figure 2.2.

The experimental Hall B hosts the CEBAF Large Acceptance Spectrometer for operation at 12 GeV (CLAS12)[19], a spectrometer developed by an international collaboration of 48 institutions. CLAS12 is based on a dual-magnet system, constituted by a torus magnet (forward region) and a solenoid magnet (target region), and it is designed to provide efficient detection of charged and neutral particles over a large fraction of the solid
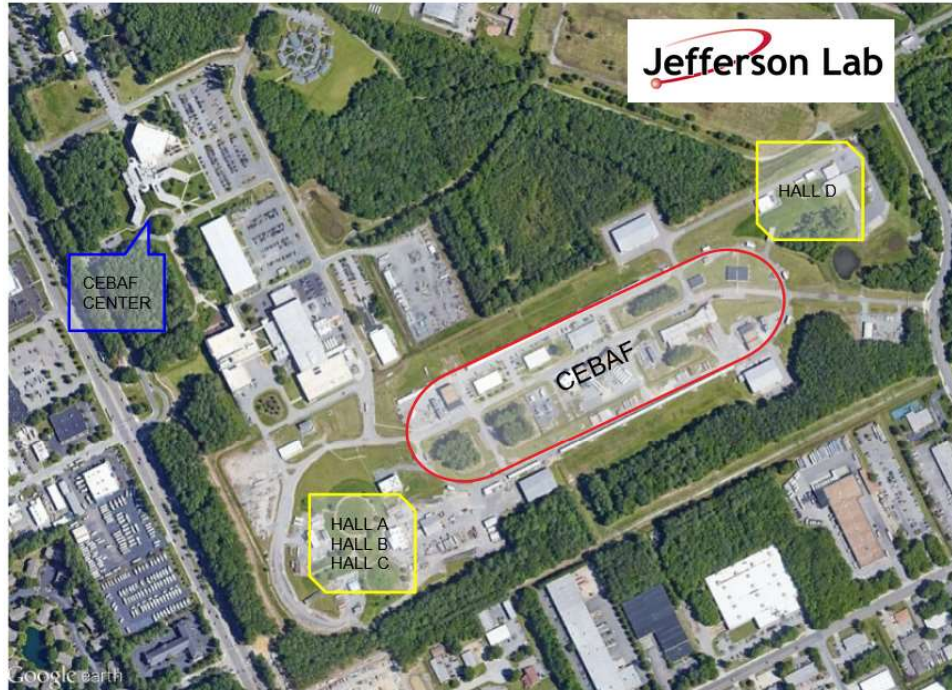
Figure 2.1: The JLab site

Figure 2.2: The CEBAF and experimental halls scheme

angle. The main goals of the CLAS12 physics program are:

- Nucleon structure studies using exclusive and semi-inclusive deep inelastic scattering processes by mapping the Generalized Parton Distributions (GPDs)[1] and Transverse-Momentum-Dependent (TMD)s;

- Precision measurement of structure functions and forward parton distribution at high x_B;

- Elastic and transition form factors at high momentum;

- Hadronization and color transparency;

- Hadron spectroscopy, studying heavy baryons and mesons with ordinary and exotic quantum numbers.

The magnets

The solenoid (Figure 2.3a) is made by self-shielded superconducting coils surrounding the beamline and used to generate a magnetic field primary in the beam direction. This design allows us to achieve the physics requirements of shielding the Moeller electron background, tracking particles with large angles, and providing a uniform field in the center to operate dynamically polarized proton and deuteron targets. The solenoid generates a 5 T field at its center at the maximum current.

The torus (Figure 2.3b) magnet comprises six identical superconducting coils, symmetrically arranged to obtain a toroidal field around the beamline. The geometrical coverage seen from the target is between 5° and 40°. The peak field is 3.58 T, while the field is zero at the center for reasons of symmetry. It is designed to bend high-energy charged particles while allowing passage of the scattered primary beam.

2.1.1 The detector

CLAS12 can be divided into the Central Detector (CD) and the Forward Detector (FD).
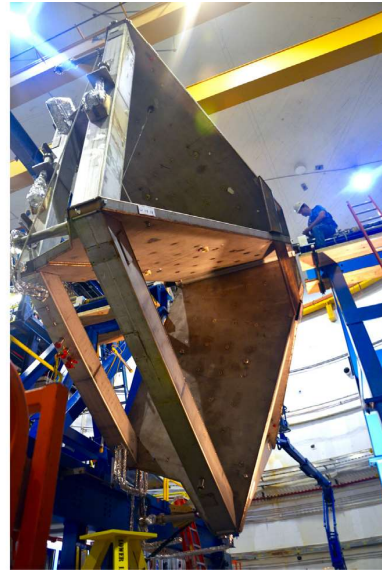
The Central Detector

The CD is designed to detect particles covering the polar angle between 35° and 125° and almost the whole azimuthal angle. The CD is placed inside the solenoid magnet. The tracking and the measure of the momentum are provided by the Central Vertex Tracker (CVT), while the charged particle identification is entrusted to the Central Time-Of-Flight (CTOF). Moreover,

---

[1]GPDs are a different way of accessing the nucleon structure. They are like tomographic slices of the form factors at a fixed value of the momentum fraction x_B

(a) CLAS12 solenoid   (b) CLAS12 torus

Figure 2.3: The CLAS12 superconducting magnets.

the CD includes two neutron detectors, the Central Neutron Detector (CND) and the Back Angle Neutron Detector (BAND). These detect neutrons with momentum up to $1.25\,\mathrm{GeV}$ and polar angle up to $175°$.

The Forward Detector

The Forward Detector (FD) covers polar angles between $5°$ and $35°$, with tracking, particle identification, and momentum measurement provided by different detectors. The FD structure is based on the torus magnet, so it is divided into six sectors that are identical in dimensions and almost identical in composition. All the sectors include three regions of Drift Chamber (DC) for tracking and two calorimeters, the Electromagnetic Calorimeter (EC) and Pre-shower Calorimeter (PCAL) for identification and kinematical reconstruction of electrons, photons, and neutrons. The only differences between sectors regard the Particle Identification (PID) components. Indeed, all six are equipped with a High Threshold Cherenkov Counter (HTCC) and a Forward Time-Of-Flight (FTOF), four sectors host a Low Threshold Cherenkov Counter (LTCC), and the other two a Ring Imaging Cherenkov (RICH) detector; more details about the PID are discussed in the following. Moreover, the FD includes the Forward Tagger (FT) to extend the capability of detecting electrons and photons at very forward polar angles between $2.5°$ and $4.5°$, consisting of a calorimeter, a hodoscope, and a micro-strip gas tracker.

The FD Particle Identification

The PID, particularly the capability to distinguish charged hadrons and leptons, plays a crucial role in QCD studies with flavor sensitivity. Indeed, aiming to perform SIDIS measurements, the precise identification of the final states particles acquires great importance. The following detectors concur in the PID:

- The Forward Time-Of-Flight (FTOF) measures the time-of-flight of charged particles from the production target. The system is designed to reach an average time resolution of 80 ps to distinguish pions and kaons up to 3 GeV.

- The Low Threshold Cherenkov Counter (LTCC) is a Cherenkov counter that uses C_4F_{10} as a radiator; it allows the tag of the charged pions up to 3.5 GeV.

- The High Threshold Cherenkov Counter (HTCC) separates the electrons and positrons with momenta below 4.9 GeV from charged hadrons. It operates in dry CO_2 gas at 1 atm pressure.

- Two Ring Imaging Cherenkov (RICH) detectors were added (the first in 2018 and the second in 2022) in two opposite sectors to improve the identification of charged kaons in higher momentum range inaccessible with the FTOF and LTCC. They are based on the measurement of the Cherenkov angle of the photons emitted by the charged particle passing through an aerogel radiator, which, combined with the kinematic information, allows the separation of the hadron species.

A scheme of the RICH and LTCC positions is shown in Figure 2.4. The author was directly involved in the assembly of the second module of the RICH, in the efficiency studies of the first module, and in the first analysis of SIDIS based on the RICH kaon identification.

2.2 The CLAS12 Ring Imaging Cherenkov

In 2018, a first Ring Imaging Cherenkov (RICH) detector [40] was incorporated into the CLAS12 spectrometer at JLab. A RICH detector exploits the Cherenkov photons produced by a charged particle crossing a radiator with a speed greater than the speed of light in that medium to identify the velocity of the particle. This information, combined with the momentum measured by other detectors, allows to identify the mass of the particle. The Cherenkov effect is described by

$$\cos\theta_{Ch} = \frac{1}{\beta n(\lambda)} \tag{2.1}$$
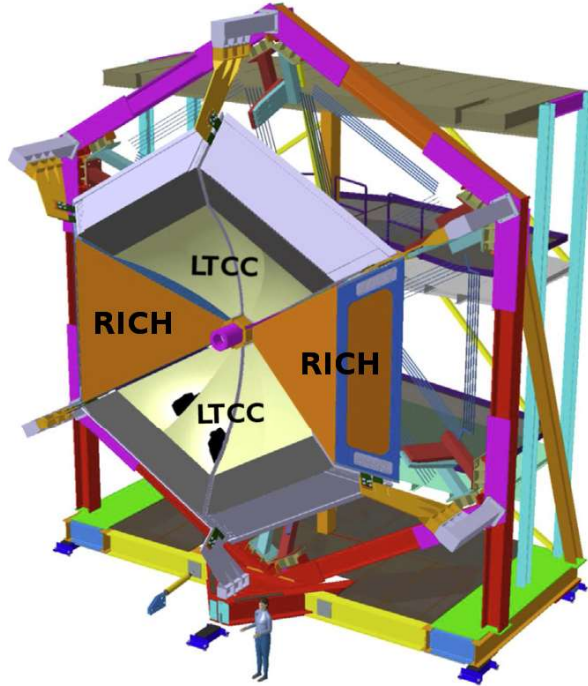
Figure 2.4: Scheme of the RICH and LTCC detectors position in CLAS12.

where θ_{Ch} is the opening angle of the photon from the particle trajectory, β is the particle's speed, and $n(\lambda)$ is the refractive index of the medium depending on the wavelength. After a gap region, the projection of the Cherenkov cone into an active surface is the so-called "ring", which has to be detected by light detectors operating in single-photon mode. A generic RICH functioning scheme is shown in Figure 2.5a. The CLAS12 RICH was explicitly designed to facilitate efficient kaon identification in the momentum range between $3\,\mathrm{GeV}/\mathrm{c}$ and $8\,\mathrm{GeV}/\mathrm{c}$. Indeed, the original PID system based on FTOF, LTCC, and HTCC does not provide sufficient separation in this momentum range between kaons, pions, and protons for effective SIDIS studies on kaons. In 2022, a second module was installed, identical to the first. Figure 2.18b shows CLAS12 with the two RICH modules.

2.2.1 RICH design

According to the CLAS12 Monte Carlo studies, the kaons identification needs to achieve a rejection factor for pions in the order of $1 : 500$, corresponding to a separation of 4σ between pions and kaons. The separation power is defined as the difference of the detector response R for pions and kaons divided by

(a) Functioning scheme of a generic RICH detector

(b) On top direct imaging; on bottom imaging after one or more reflections on the mirrors.
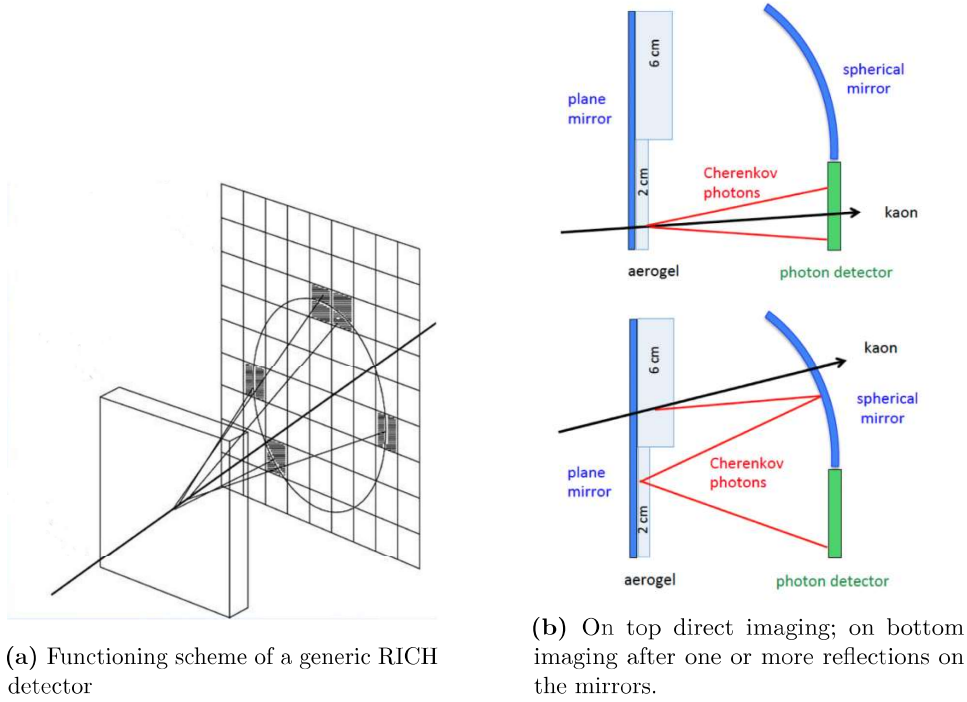
Figure 2.5

the mean of the resolution

$$n_\sigma = \frac{R_\pi - R_K}{\langle \sigma_{\pi,K} \rangle}.$$ (2.2)

As shown in Figure 2.6, the only possible radiator is the silica aerogel, which has a very low macroscopic density and a refractive index between the gas and the liquids. The RICH has to fit inside the Forward Carriage of CLAS12, which imposes several constraints: a projective geometry, a limited depth of $1.2\,\mathrm{m}$, and $\sim 4.5\,\mathrm{m}^2$ entrance windows. Based on the simulation, the RICH is designed to integrate the aerogel radiators, visible light photon detectors, and a focusing mirror system in a compact hybrid-optics design. The mirrors allow the reduction of the photon detector area to $\sim 1\,\mathrm{m}^2$, minimizing the cost and the impact on the downstream detectors. Depending on the polar angle of the incident particles, the photons can hit the photo-detection area directly, as shown in Figure 2.5b (top), or after multiple reflections with a second passage through the radiator, as shown in Figure 2.5b (bottom). To minimize the total material budget, the mechanical structure is made almost entirely of light composite materials, in particular carbon fiber. A complete detector scheme is shown in Figure 2.7.
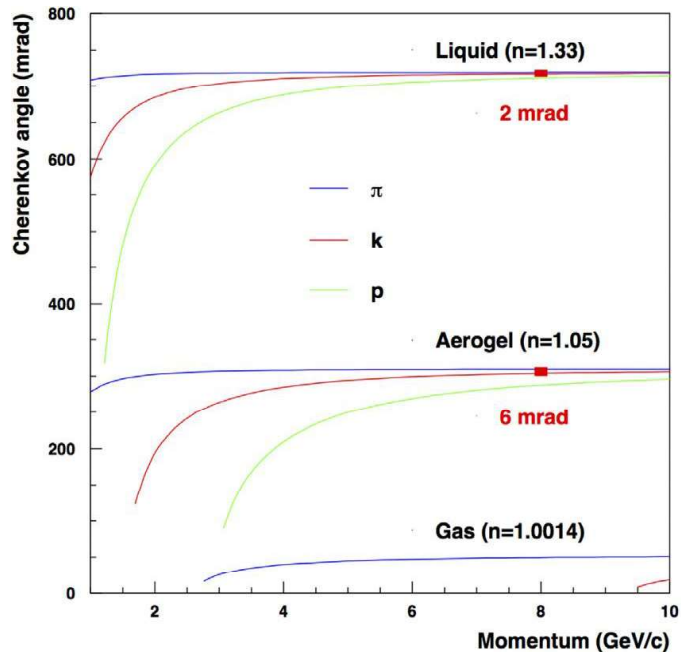
Figure 2.6: Expected Cherenkov angle for different hadron as a function of momentum for different radiators.

2.2.2 The radiator

The radiator selected for the RICH was the silica aerogel, the only effective choice in the wanted $3 \div 8\,\text{GeV}$ momentum range, as shown from the plot in Figure 2.6, where the expected Cherenkov angle for different hadrons is plotted as a function of the particle momentum. The aerogel is an amorphous solid network of SiO_2 nanosphere, and it has a very low macroscopic density and a refractive index intermediate between gas and liquid radiators. The aerogel was produced by Budker and the Boreskov Institute of Nuclear Physics (Russia), which made all the 102 tiles of different shapes and thicknesses needed for each detector module. The tiles were assembled into two sections. The first, made of one layer of 2-cm-thick tiles, covers the region between the beam pipe up to the polar angle of 17.5°. The second region covers the polar angle between 17.5° and 26° and is made of two layers of 3-cm-thick tiles. Most tiles are squared $20 \times 20\,\text{cm}^2$ bricks, but triangular, trapezoidal, and pentagonal shapes became necessary on the edges to cover the entire triangular entrance window. Each tile was tested [41] to determine the side length, thickness, and surface planarity. Also, the optical parameters were measured, particularly the refractive index at the reference wavelength of $400\,\text{nm}$ and the light transmission as a function of the wavelength. Using the Hunt parametrization [42], the parameters of transparency A_0, clarity C, and scattering length at $400\,\text{nm}$ Λ_S were extracted. From these measurements,

26
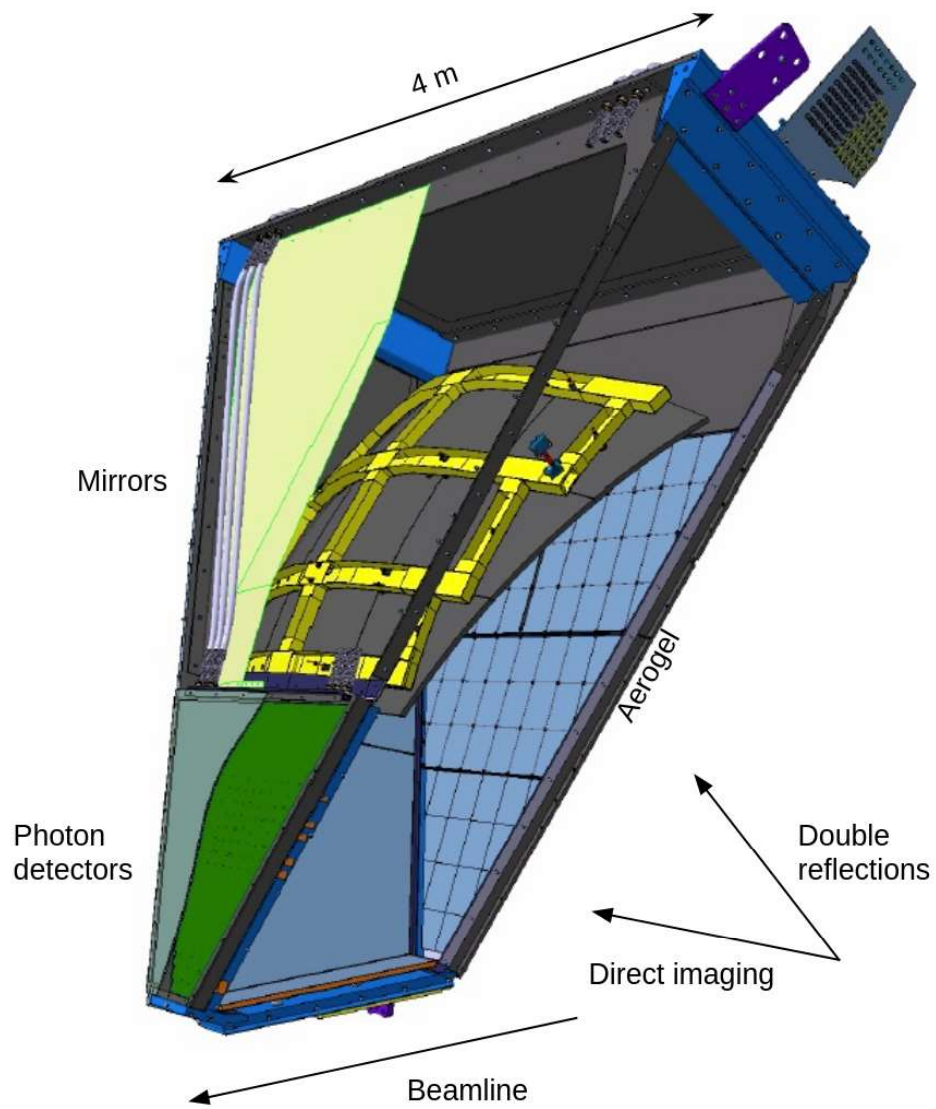
Figure 2.7: Sketch of the full RICH: the aerogel tiles, the structure supporting the spherical mirrors, and the photo-detection plane are indicated.

the expected mean photon yield is 19 photoelectrons (p.e.) for the 2-cm-thick layer and 25 p.e. for the 6-cm-thick layer.

2.2.3   The mirror system

According to the simulation, the mirror system was designed to minimize the loss of photons and direct most of them to the photon detector. A drawing of the entire mirror system is shown in Figure 2.8.

The spherical mirror

The spherical mirror comprises ten sub-mirrors produced by the *Composite Mirror Applications* company [43]. It covers a total surface of $3.6\,m^2$ and has a curvature radius of $2.7\,m$. This mirror is placed in front of the entrance window to collect the photons produced by particles entering with a large polar angle. The accuracy of each sub-mirror spherical surface was quantified via the spot size measurement, illuminating the mirror with a point-like source and observing the size of the reflected spot with a CCD camera in its center. The size spot is quantified by D_0, the minimum diameter containing 90% of the reflected light, which is related to the angular resolution by

$$\sigma_\theta = \frac{D_0}{8R} \qquad (2.3)$$

where R is the curvature radius. The mirror mechanical substrate is made by a sandwich of two carbon fiber layers with a honeycomb core that achieves a high rigidity and a low material budget of $0.01X_0$. The mirrors were coated with a reflective SiO_2 layer by the *Evaporated Coating* company [44]. The reflectivity of the mirrors is measured to be between 88% and 90% in the $300 - 700\,nm$ wavelength range of interest.

The planar mirrors

There are seven planar mirrors, two placed on each side of the detector, one on the bottom, and two on the front panel supporting the aerogel, covering a total surface of $6.5\,m^2$. They were produced by the *Media Lario* company [45], which is used to work for terrestrial telescope applications. The mirrors are made of two skins of glass glued on an aluminum honeycomb core; the front mirror skins are $0.7\,mm$ thick to reduce the mirror material budget to $\sim 0.01X_0$ in the detector acceptance, while the lateral mirror skins have a more standard $1.6\,mm$ thickness. The reflectivity of the planar mirrors has been measured to be greater than 90% in the $300 - 700\,nm$ range of wavelength and shows a maximum of about 95% at $400\,nm$.
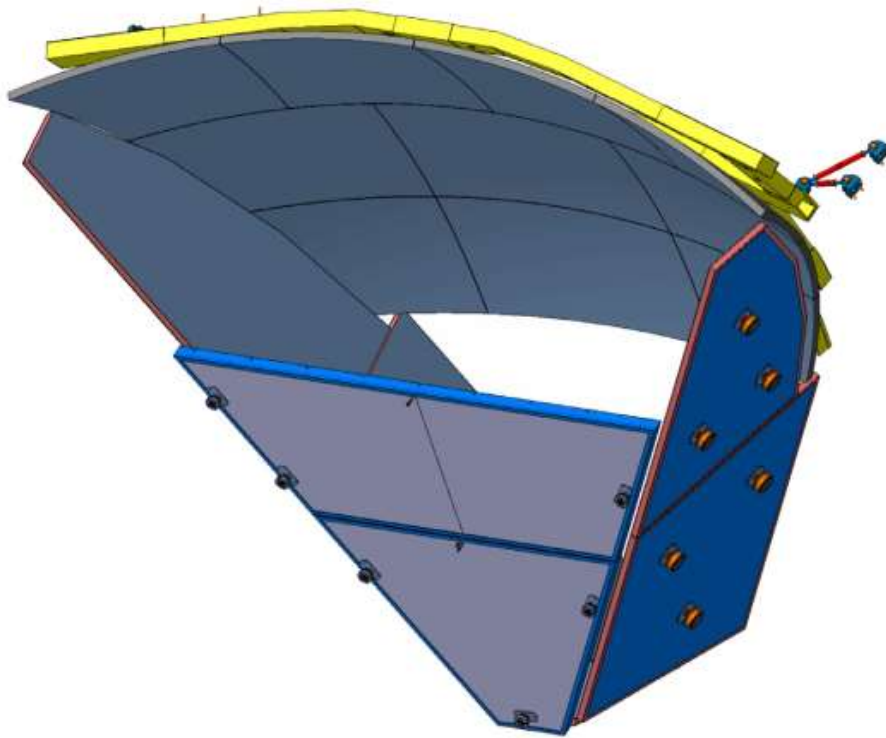
Figure 2.8: RICH mirror system draw. The spherical mirror has ten different spherical mirrors reflecting the light backward. Two mirrors upstream on the aerogel reflect the photons a second time in the direction of the MAPMTs, as shown in figure 2.5b. To minimize the photon loss, two planar mirrors on each side and one on the bottom surround the rest of the RICH module.

2.2.4 The photon detector

The mirrors were designed to reduce the photo-detection area to $\sim 1\,\mathrm{m}^2$, in the region close to the beamline where most of the particles are produced and with the most demanding high momenta concentration.

The photo-sensor

To make imaging possible, the photo-sensor has to work efficiently in the Single PhotoElectron (SPE) regime and be sensitive to visible light (to match the aerogel emission spectrum). Moreover, it must have the spatial resolution required to achieve the designed angular resolution, provide an active area with minimal dead space, and be insensitive to the low torus fringe field where the RICH readout is located (estimated to be no more than $3.5\,\mathrm{G}$). The Hamamatsu flat-panel Multi-Anode Photomultiplier Tube (MAPMT) H8500, an 8×8 array of $6 \times 6\,\mathrm{mm}^2$ pixels covering a $5 \times 5\,\mathrm{cm}^2$ area, was initially selected as photo-sensor. However, it was not designed for the SPE regime. Just after the start of the RICH construction, Hamamatsu released the H12700 MAPMT, which has the same layout and an optimized dynode structure for SPE. The first RICH combines 80 H8500 and 311 H12700 for a total of 391 photo-sensors, while the second module is fully equipped with H12700. This configuration results in 25024 pixels covering the $\sim 1\,\mathrm{m}^2$ trapezoidal active area of each RICH module. Figure 2.9a, shows a view of the MAPMTs side of the electronic panel.

The readout electronics

The front-end electronics is organized in compact modules called tiles serving two or three MAPMTs. The tile scheme is shown in Figure 2.10. The front-end electronics is intended to ensure a 100% discrimination efficiency at $\frac{1}{3}$ of the average photoelectron signal level, 1 to 4 gain spread compensation, and time resolution of the order of $1\,\mathrm{ns}$ to distinguish direct from reflected hits. Additionally, it has to sustain a $20\,\mathrm{kHz}$ trigger rate with $8\,\mathrm{\mu s}$ latency and negligible dead time. A stack of three different boards makes each readout unit:

- The adapter board provides the electrical connectivity of the sensors with the readout, preserving the light and gas tightness when the electronic panel is mounted in the detector. It also distributes the power to the MAPMTs, with a nominal bias of $-1000\,\mathrm{V}$.

- The ASIC board mounts two or three Multi-Anode ReadOut Chip (MAROC) chips [46], a 64-channel microcircuit dedicated to the processing of MAPMTs signals.

(a) MAPMTs side

(b) Front-end electronic side
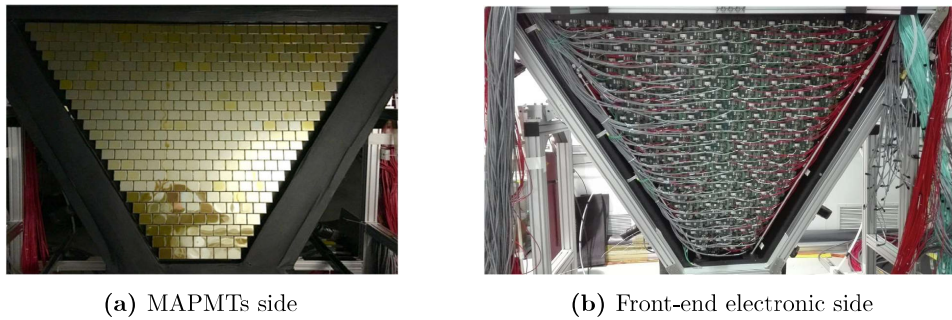
Figure 2.9: The RICH electronic panel.
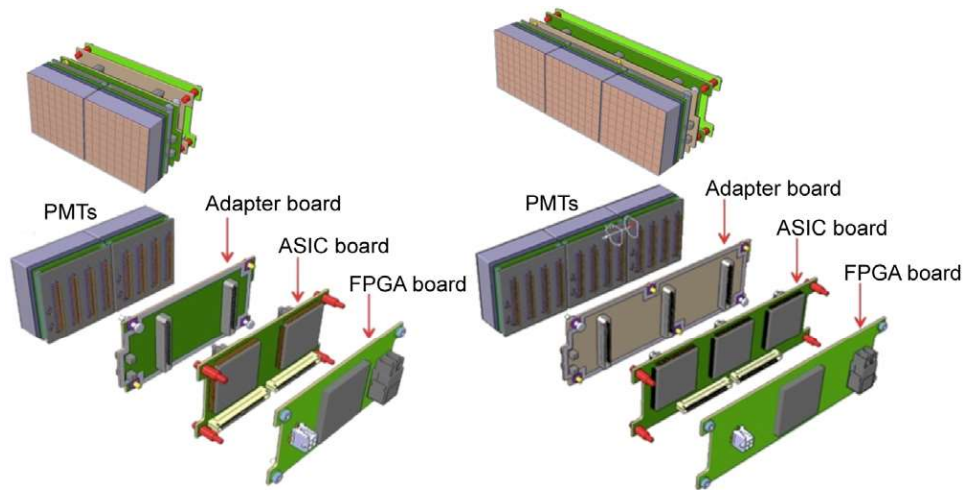
Figure 2.10: Scheme of the front-end electronic tiles serving two (left) or three (right) MAPMTs.

- The FPGA board hosts a Xilinx7 FPGA chip responsible for configuring and reading the MAROC chips, distributing the trigger, and interfacing with the DAQ system.

To connect the readout system, three kinds of cable are in use for each tile: the low-voltage cables to power the FPGA and the digitization chain, the high-voltage cable to power the MAPMTs, and the optical fiber for the communication between the FPGA and the DAQ system. The electronic panel was completed with a grounding grid, which attenuates the electronic noise, and the cooling system, based on a flow of compressed dry air that allows to maintain the temperature of the FPGA below the critical value of 75 °C. A picture of the full readout electronics of the RICH is reported in Figure 2.9b.

2.3 The assembly and commissioning of the second module of the RICH

In the spring of 2022, the author was directly involved in the assembling the second module of the RICH, in particular focusing on the electronic panel mounting and the installation of the detector inside the CLAS12 experiment. The assembling process before the installation was performed inside a clean room at JLab, and each subsystem was mounted into the detector structure after the completion of the relative characterization tests. The expert of mechanics from INFN Frascati took care of the assembly of the RICH vessel (see Figure 2.14a), which has to sustain the entire detector structure. The spherical mirrors were characterized and then mounted in their support structure inside the vessel, while the planar mirrors were directly mounted on the vessel's walls (Figure 2.14d). The characterization includes measurements of the reflectivity in several points and of the point-like reflected spot size (Figures 2.12 and 2.13). The ten spherical sub-mirrors were aligned using a point-like source and converging the reflected spots on the same point (Figure 2.14c). The hydrophobic aerogel was purged with a flux of nitrogen and mounted on the inner side of the frontal panel, in the section with (Figure 2.11a) and without (Figure 2.14b) mirrors. The INFN Ferrara team, including the author, worked mainly on the electronic panel, starting from mounting the adapter boards on the inner side and connecting them with the ASIC boards on the other side (Figure 2.14e). Then, they added the FPGA boards to the ASIC boards and cabled all the 138 tiles (Figure 2.14f). After completing this step, the 391 MAPMTs were put in place by members of the Ferrara team, JLab and Duquesne University. All the readout units were connected to the power and DAQ system and tested (Figure 2.15). Under the supervision of the Frascati and Ferrara experts, the electronic panel was moved into the RICH vessel and tested again to ensure all the readout units worked correctly.

The last step was to place the frontal panel with the aerogel layer into the detector; the picture in Figure 2.11b was taken during this operation. This operation was particularly critical because when the aerogel is placed on its supports it should never be turned face down. A CCD camera and a small portable light were placed inside the detector to check if any problem occurred during the moving phase. The completed RICH was tested for light leaks, which can cause problems for SPE, and gas leaks because the inner humidity needs to be minimized to maintain the aerogel properties. At the beginning of June 2022, the RICH was moved into Hall B (Figure 2.16), about 1 km from the clean room, using a truck with a special trolley. The assembly and transportation were made with the detector in a horizontal position; in Hall B, it was rotated vertically, with the short side on the bottom and the large on top. Then, it was rotated clockwise along the axis that passes through the
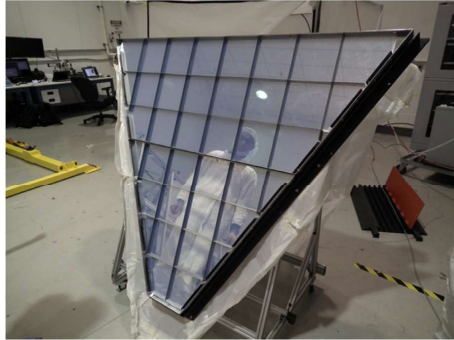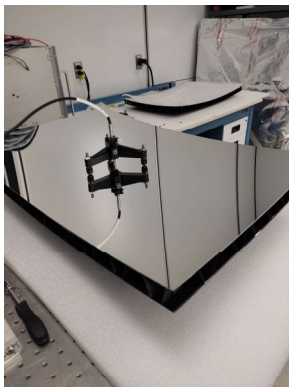
(a) The 2-cm-thick section of the aerogel mounted on the two frontal mirrors.
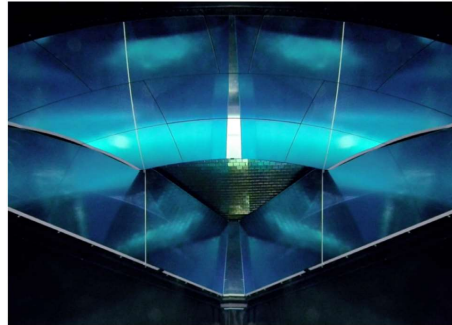
(b) Inside the RICH detector, the mirror system is seen from the entrance panel. From the top, clockwise, there are the ten spherical sub-mirrors, the two right mirrors, the bottom mirror, and the two left mirrors. At the center, the MAPMTs are visible.
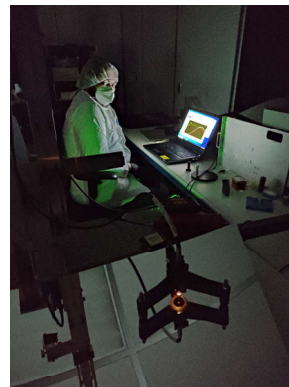
Figure 2.11
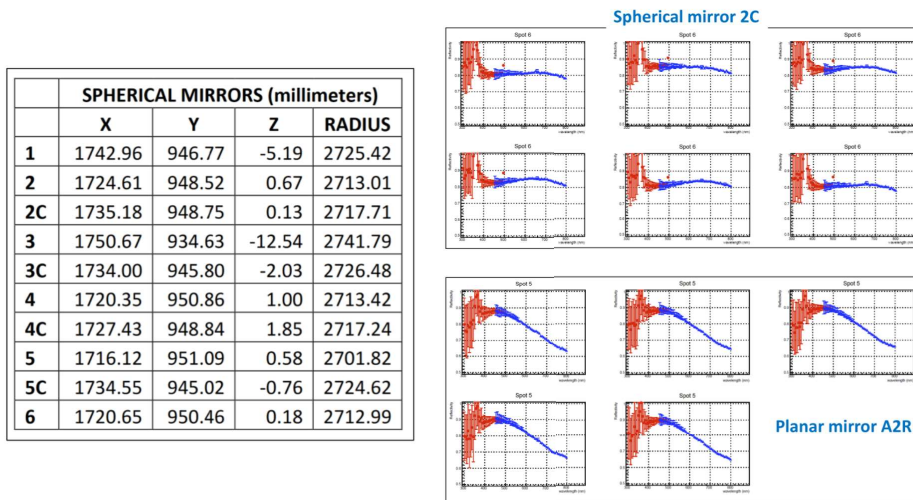

(a) Reflectivity measurement apparatus.
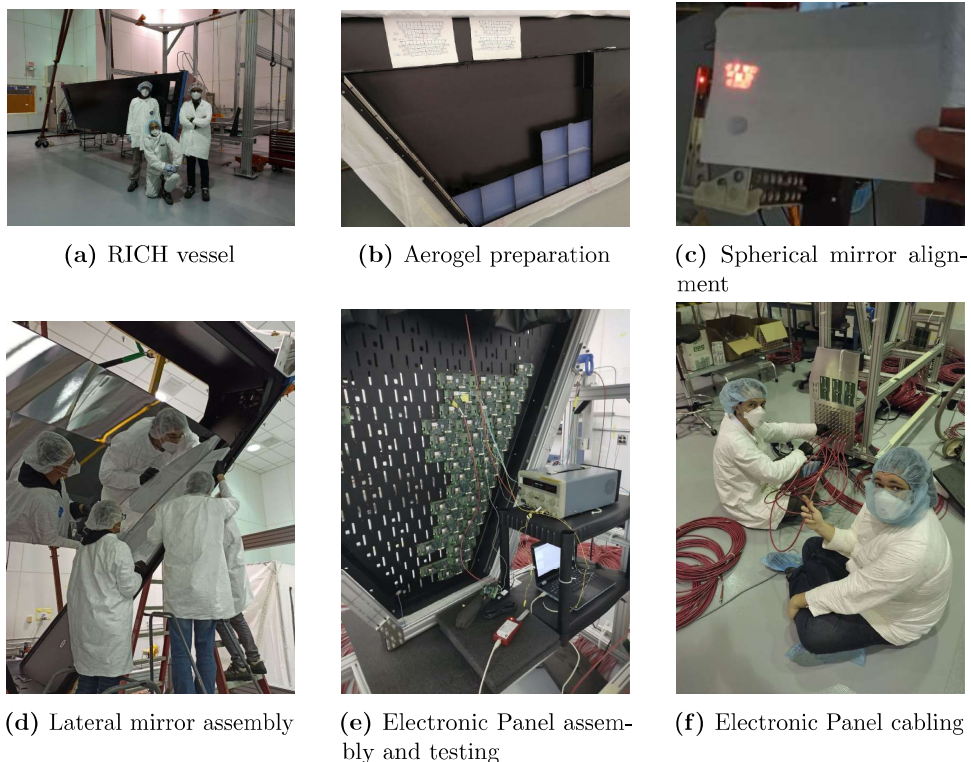

(b) Point-like reflected spot size measurement station.

(c) The author during the measurement.

Figure 2.12

SPHERICAL MIRRORS (millimeters)			
	X	**Y**	**Z**	**RADIUS**
1	1742.96	946.77	-5.19	2725.42
2	1724.61	948.52	0.67	2713.01
2C	1735.18	948.75	0.13	2717.71
3	1750.67	934.63	-12.54	2741.79
3C	1734.00	945.80	-2.03	2726.48
4	1720.35	950.86	1.00	2713.42
4C	1727.43	948.84	1.85	2717.24
5	1716.12	951.09	0.58	2701.82
5C	1734.55	945.02	-0.76	2724.62
6	1720.65	950.46	0.18	2712.99

Figure 2.13: Results of mirrors characterization. On the left: curvature radius of spherical mirrors; on the right: reflectivity measured as a function of wavelength in several points for one spherical and one planar mirror.

(a) RICH vessel

(b) Aerogel preparation

(c) Spherical mirror alignment

(d) Lateral mirror assembly

(e) Electronic Panel assembly and testing

(f) Electronic Panel cabling

Figure 2.14

(a) Screenshot from the CLAS12 Slow Control system, which regulates the detector's power supply, during the first turning on of the full electronic panel.

(b) Thermal imaging camera picture of the electronic boards taken during the first functionality tests.
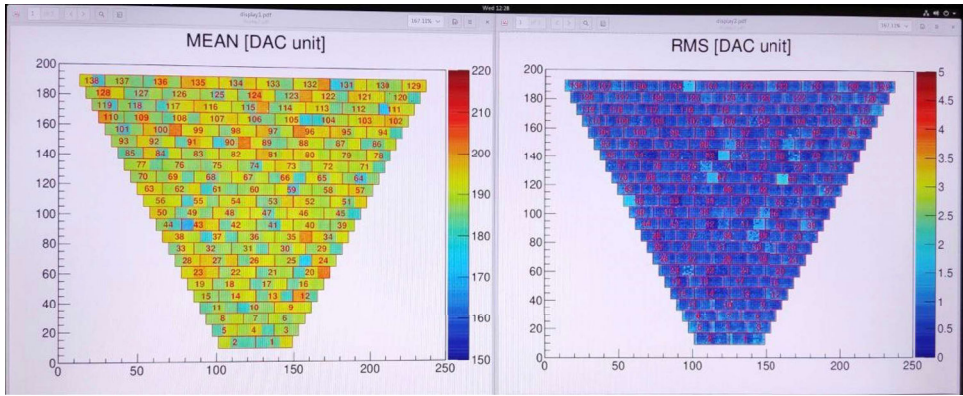
(c) Screenshot of the scaler plots taken during the first tests.
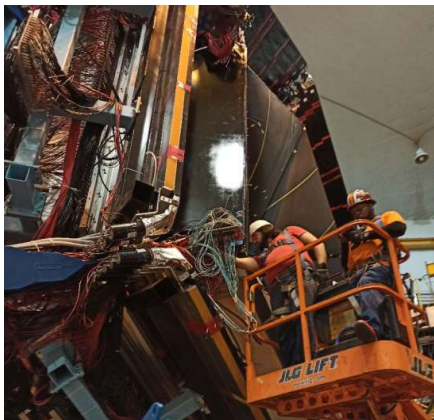
Figure 2.15
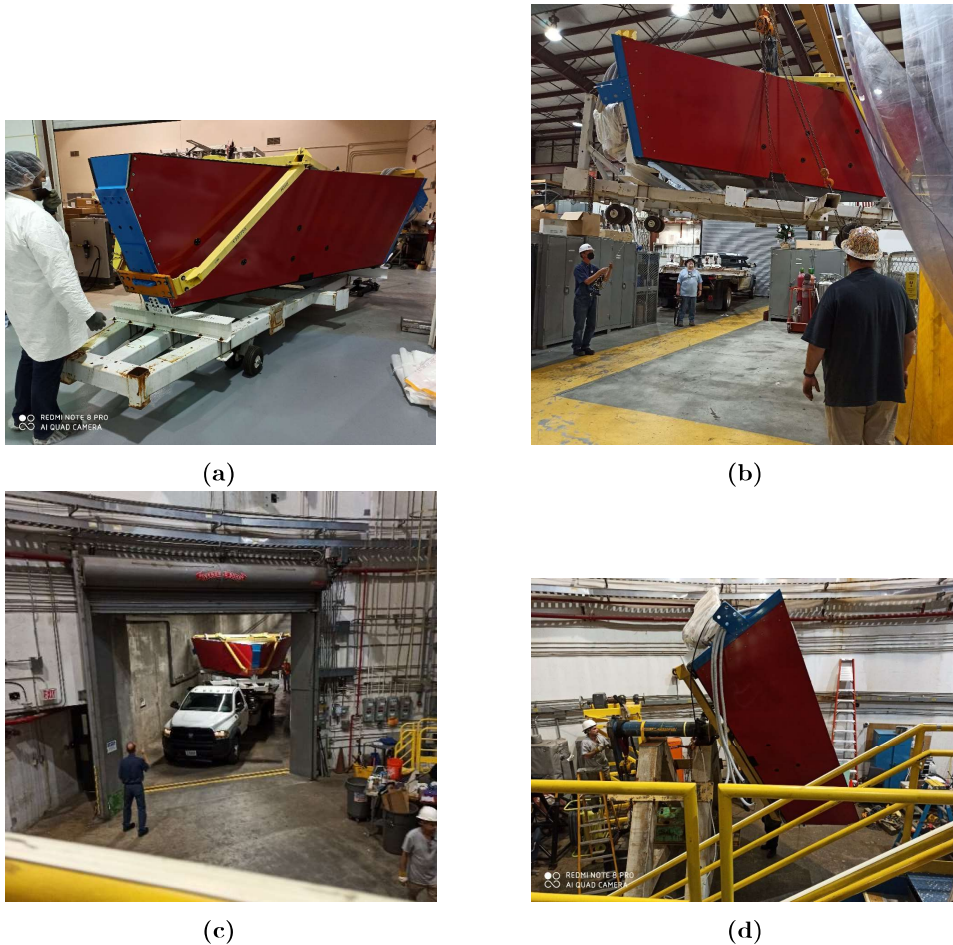
Figure 2.16: Moving of the RICH from the clean room to Hall B.

detector barycenter to place it in the final orientation with the short side on the right, close to the beamline, and the large side on the left. Finally, the RICH was raised to take its place inside the CLAS12 spectrometer. Since the moving phase was another critical step in the installation, the internal CCD camera was used to check again that no problem occurred to the aerogel. Figure 2.17 shows a picture taken inside the RICH after the installation.

Finally, the author was directly involved in cabling the RICH to the infrastructure of the CLAS12 experiment (Figure 2.18a). The picture of the complete array of RICH and LTCC modules of CLAS12 after the second RICH module installation is reported in Figure 2.18b. The RICH was included in the CLAS12 DAQ chain, and all the calibration and control procedures were extended from the first module. The first slow-control signals from the two modules are reported in Figures 2.18c and 2.18d.

Figure 2.17: View of the aerogel inside the RICH after its installation in Hall B.
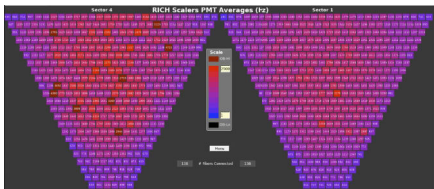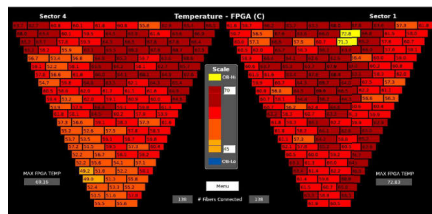

(a) Cabling the RICH
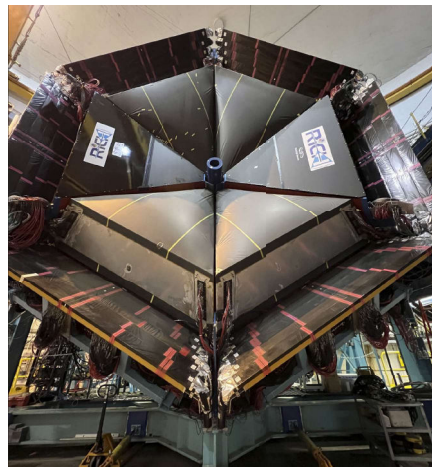
(b) Section of CLAS12 after installing the two modules of the Ring Imaging Cherenkov detector.

(c) First scaler map of the two modules.

(d) First temperature map of the two modules.
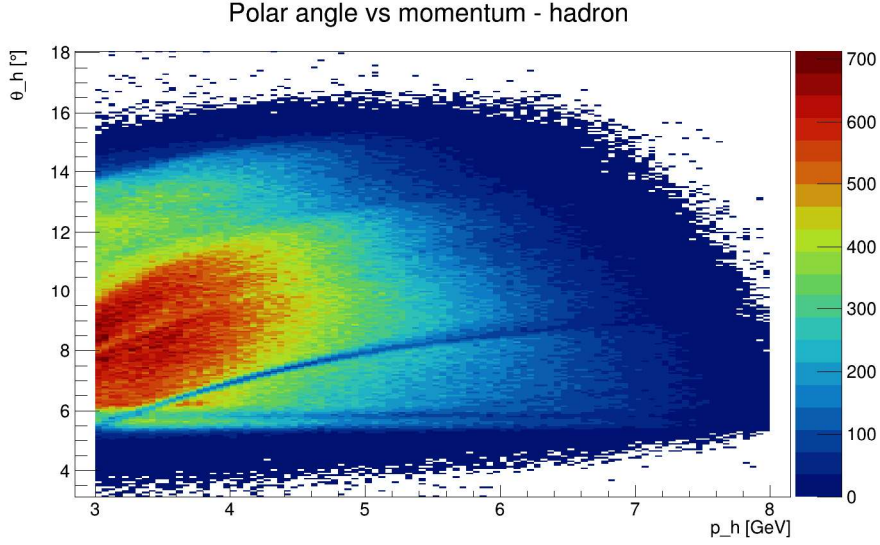
Figure 2.18

2.4 RICH performance

The main goal of the RICH was to enhance the kaon identification and improve the pion rejection. As a consequence, the first study on the detector performances aims to evaluate the percentage of correctly identified pions and the percentage of pions misidentified as kaon, which was not a negligible number using the standard PID of CLAS12. The purity of the sample provided by the RICH can be studied by comparing the missing mass of final states like eH^+X selected using the PID of CLAS12 (without the RICH) or the PID provided by the RICH. This study does not evaluate the absolute detector's efficiency but its capability to provide a kaon sample with small pion contamination. It defines a sort of preliminary quality assessment for identifying kaon based on the RICH variables that will be used in the analysis described in the next Chapter.

2.4.1 Data sample

The analysis was performed on a control sample containing data of the scattering of the 10.2 GeV electron beam off the Hydrogen target. The selection criteria applied are similar to the ones used in the SIDIS analysis described in Chapter 3 but less refined. The preliminary selection is based on the request that the electron was a trigger particle, its momentum was greater than 1.5 GeV, and that the reduced χ^2_{track}/NDF of the hadron track is less than 8. To study the RICH performance in the design working range, the hadron momentum was selected to be in the momentum range from 3 to 8 GeV. Aiming to evaluate the RICH performances and compare them with CLAS12 PID without the RICH, an additional request was that both the RICH and CLAS12 event builder (which still does not include the RICH) provide a hadron identification. The sample that survived these cuts consists of $\sim 5.1 \times 10^6$ events. Currently, the range of the hadron polar angle is partially limited because the alignment of part of the spherical sub-mirrors in the reconstruction code has yet to be finalized. The polar angle covers values up to $\sim 15°$. The distribution of the polar angle and momentum of the hadron sample used for the analysis is shown in Figure 2.19.

Two selections were applied to the detector-related variables to obtain a clean sample of kaons using the RICH. The first is the request to reconstruct at least three photons so that the ring can be well-defined. This selection criterium cuts $\sim 18.7\%$ of the events in the sample. The second requirement is based on a specific RICH quality variable that can be used to evaluate the reliability of the identification. A binned maximum likelihood [47] is defined (except for a constant) assuming a binned Probability Density Function

Figure 2.19: Polar angle and momentum of the hadron used for the study on the pion contamination of the kaon sample.

(PDF) with Poisson probability

$$\mathcal{L} = \prod_{i=1}^{N} \frac{\mu_i^{n_i}}{n_i!} e^{-\mu_i} \tag{2.4}$$

where n is the observed number of photons, μ the expected number of photons, θ the parameter, and N the total number bins. The maximum likelihood highlights the best hypothesis. Defining λ as the ratio of the likelihood with respect to an ideal model corresponding to the measurement, it provides a χ^2-like estimator of the hypothesis's goodness. The likelihood ratio is computed for any possible mass hypothesis, and the one minimizing the $-2\log\lambda$ selects the identification provided by the reconstruction software. The function to minimize is

$$\chi^2 \sim -2\log\lambda = 2(\overline{N} - N) + \sum_{i=1}^{N} \left[\frac{(\overline{\theta} - \theta_i)^2}{\sigma_\theta} \right] + \left[\frac{(\overline{t}(\theta) - t_i)^2}{\sigma_t} \right] \tag{2.5}$$

where $\overline{N}, \overline{\theta}$, and $\overline{t}$ are the expected number, Cherenkov angle, and time of the photons, while N, θ_i, and t_i are the corresponding measured quantities. This variable provides an estimation of how much the identification is reliable. In the case in which the likelihoods of two different mass hypotheses are both acceptable, the minimization of the likelihood is not enough to decide the level of confidence in the identification. To this scope, an estimation of the goodness and unicity of identification can be provided using the quantity
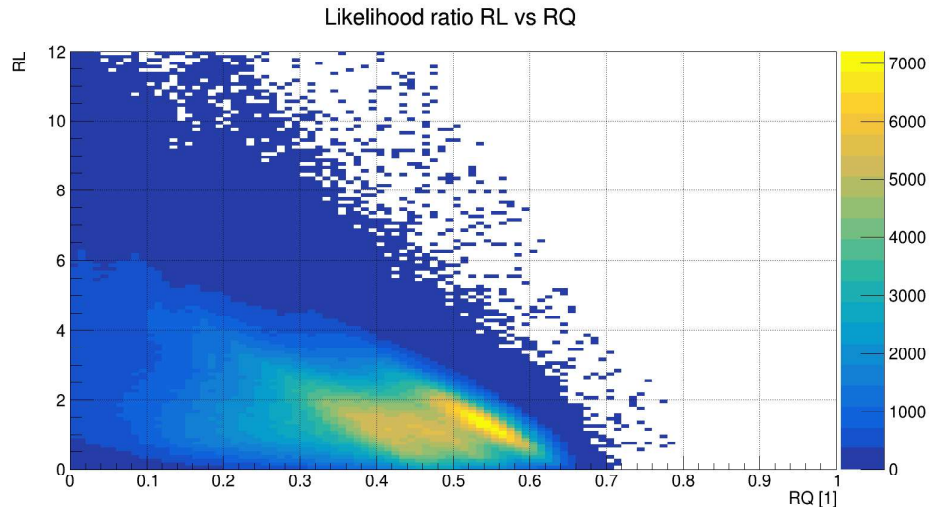
Figure 2.20: Distribution of the likelihood ratio and the RQ variables in the sample used for the RICH performance study.

defined as:

$$RQ = 1 - \frac{\lambda_{best}}{\lambda_{second\_best}}. \tag{2.6}$$

If $RQ \to 0$, the identification tends to be uncertain because the likelihoods for the two better hypotheses are very similar. If $RQ \to 1$, the best likelihood is much better to the alternative, then the identification is more reliable. There is a correlation between the likelihood ratio and the RQ, as it is shown in Figure 2.20. The number of events having a high likelihood ratio, more than 9, is very limited: checking it was less than 0.1%. Instead, the events with a low likelihood ratio and low RQ are not negligible. The distribution of the RQ quantity for the hadron sample used in this study is shown in Figure 2.21. The kaon sample purity was evaluated by applying two different conditions on the RQ variable: no selection or the request of a value larger than 0.1. The last requirement reduced the available statistics of $\sim 7\%$. Combining the two requirements on the RICH variables, the events selected by the RICH-related selections are the 77.9% of the initial sample, consisting of $\sim 4 \times 10^6$ events.

2.4.2 Analysis

The neutron peak at the missing mass of $0.94\,\mathrm{GeV}$ was used to evaluate the kaon sample purity and the pion identification efficiency. Indeed, the exclusive final state $e\pi^+ n$ is allowed, while the state $eK^+ n$ is forbidden for strangeness conservation. As a consequence, in the missing mass plot of events with a candidate kaon, the neutron peak should not be present, while it is expected in case the selected events include a pion.
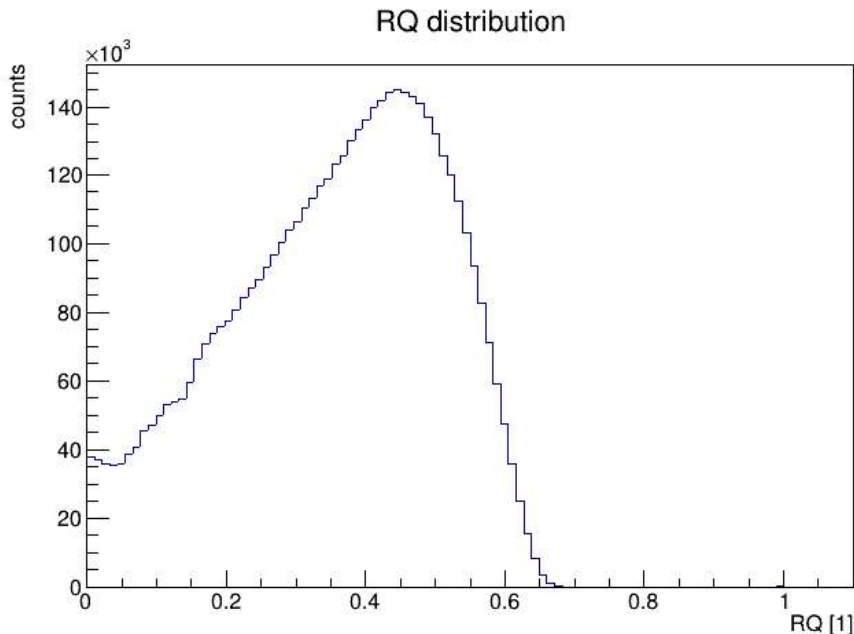
Figure 2.21: Distribution of the *RQ* variable for the hadron sample used in the RICH performance evaluation.

A first qualitative idea of the RICH performance in cleaning the kaon sample is provided by the plots in Figure 2.22 and Figure 2.23, showing the missing mass of $e\pi^+X$ and eK^+X selected using the CLAS12 PID or alternatively the RICH PID. For eK^+X candidates, the neutron peak is evident using the CLAS12 PID, while it is strongly reduced using the RICH PID. In the $e\pi^+X$ plot, the number of events is larger using the RICH instead of the CLAS12 PID: this is because a part of the hadrons recognized by CLAS12 as kaons are actually pions, and the RICH correctly identified them. For the same reason, the statistic of the eK^+X sample selected by the RICH is lower than that of the sample identified by CLAS12.

The missing mass of the eK^+X sample defined by the RICH permits us also to show the capability of the *RQ* variable of removing most of the misidentification, as shown by the clear reduction of the neutron peak in Figure 2.24.

For a quantitative evaluation of the kaon sample purity, it was decided to extract the number of neutrons associated with the peak at $0.94\,\mathrm{GeV}$ and to define the pion identification efficiency $(\eta_{\pi\to\pi})$ as
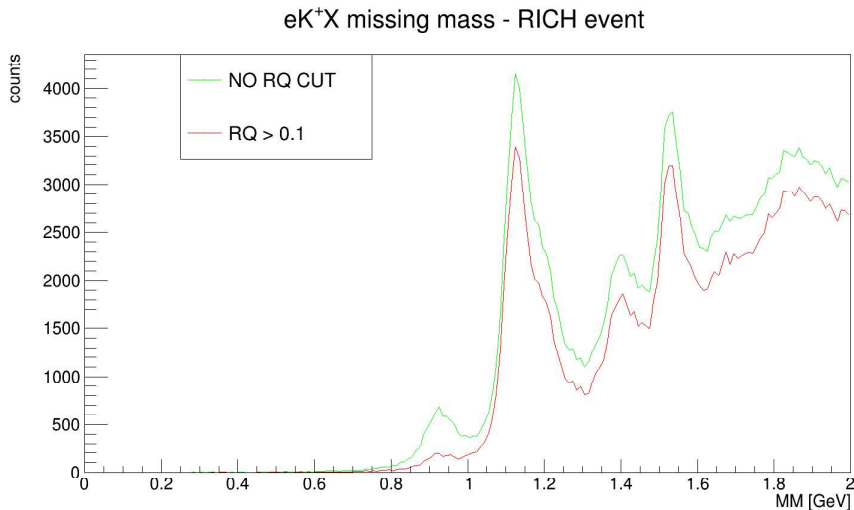
$$\eta_{\pi\to\pi} = \frac{\text{Number of exclusive neutrons in } e\pi^+X \text{ events}}{\text{Number of exclusive neutrons in } (e\pi^+X + eK^+X + epX) \text{ events}} \tag{2.7}$$
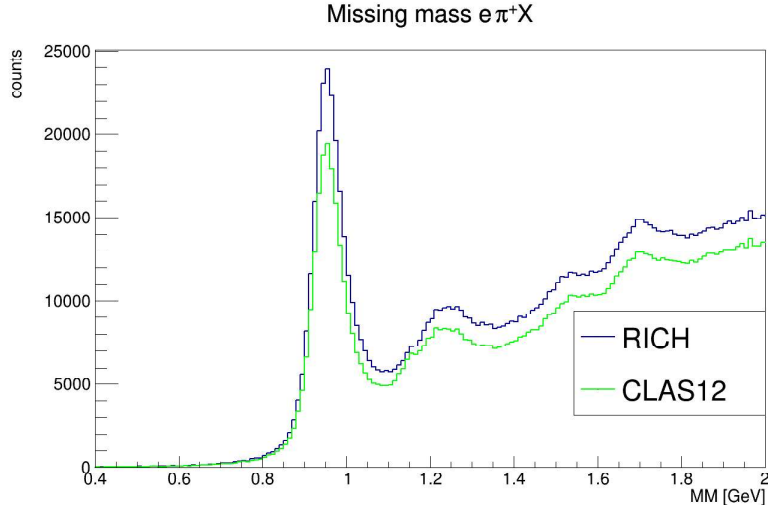
Figure 2.22: Missing mass of final state $e\pi^+X$ as identified by CLAS12 PID (green) or RICH PID (blue). The peak at $0.94\,\mathrm{GeV}$ signals the exclusive $e\pi^+n$ final state. The total number of events selected by CLAS12 is less than that selected by RICH because the first misidentified part of the hadrons as if they were kaons.
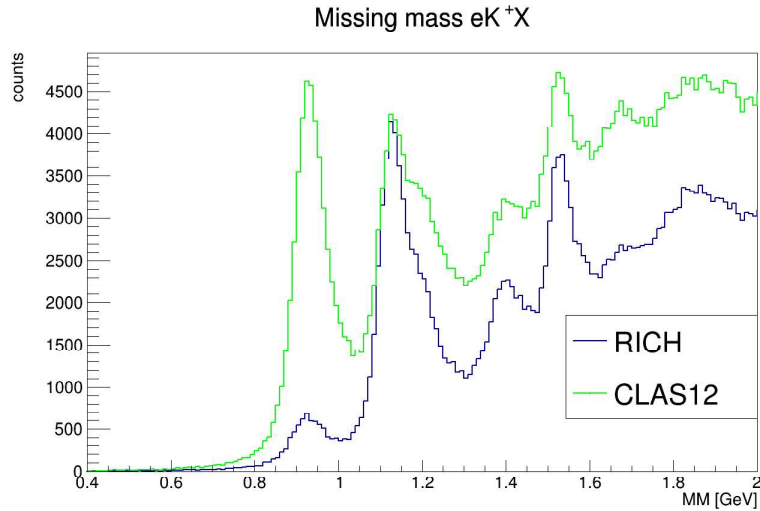
Figure 2.23: Missing mass of final state eK^+X as identified by CLAS12 PID (green) or RICH PID (blue). The clear reduction of the neutron peak at $0.94\,\mathrm{GeV}$ shows that the number of exclusives state $e\pi^+n$ decreases using the RICH; this corresponds to a lower number of pions misidentified as kaon, being forbidden the exclusive final state eK^+n. The peak close to $1.1\,\mathrm{GeV}$ is due to the contribution of exclusive states $eK^+\Lambda^0$, $eK^+\Sigma^+$ and $e\pi^+\Delta$ (pion misidentified as kaon in the last case). The total number of events selected by CLAS12 is more than that selected by RICH because the first misidentified part of the hadrons as if they were kaons.

Figure 2.24: Missing mass of final state eK^+X identified by the RICH in case of applying the cut on RQ (red) or not (green). The reduction of the neutron peak at $0.94\,\text{GeV}$ provides the qualitative idea of the RQ cut effectiveness.

and the percentage of pion misidentified as kaon ($\eta_{\pi \to K}$) as

$$\eta_{\pi \to K} = \frac{\text{Number of exclusive neutrons in } eK^+X \text{ events}}{\text{Number of exclusive neutrons in } (e\pi^+X + eK^+X + epX) \text{ events}} \tag{2.8}$$

having evaluated that the number of exclusive neutrons in the epX final state is small but not negligible.

To estimate the number of neutrons, the missing mass plots were fitted using a Gaussian function for the neutron peak, a Breit-Wigner for the Δ^0 peak, two Gaussian distributions for the Λ^0 and Σ^0. These particles are provided by the exclusive final states $eK^+\Lambda$, $eK^+\Sigma^0$, and $e\pi^+\Delta^0$. These peaks were been specifically studied during the fit parameters evaluation because they are closer to the neutron peak. The peaks associated with larger missing mass are not treated singularly but simply added as Gaussian distributions to the SIDIS background. These peaks typically result into one Gaussian centered at $1.4\,\text{GeV}$ and sometimes into one centered at $1.5\,\text{GeV}$. To describe the SIDIS background shape, a Weibull-like distribution was used:

$$bkg_{Weib}(x; p_0, p_1, p_2) = p_0 x^{p_1 - 1} \left(-\frac{x}{p_2} \right)^{p_1} \tag{2.9}$$

where x is the missing mass and p_0, p_1, and p_2 are parameters of the background. Two other background functions were tested: a second-order Chebysev polynomial and a Crystalball function. They did not show significant differences, so the Weibull background was confirmed. Three examples of fit for the pion, kaon, and proton cases are shown in Figures 2.25, 2.26, and 2.27. They
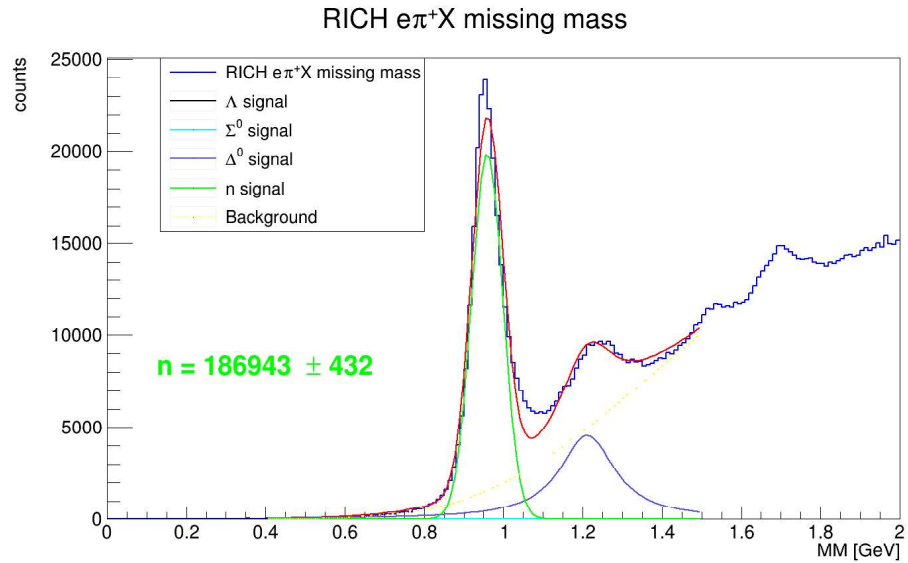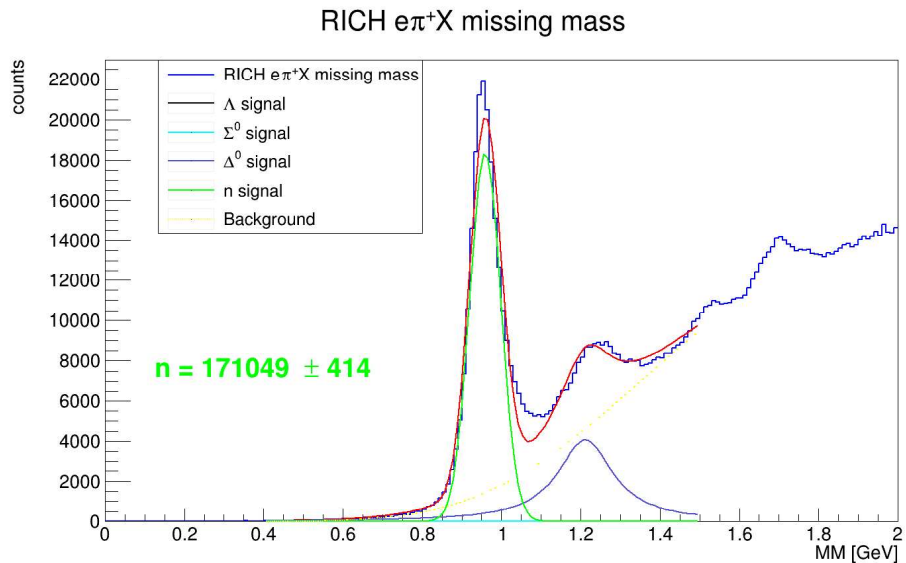
Figure 2.25: The red curve shows the fit of the missing mass plot of $e\pi^+ X$ states selected by the RICH using the Weibull-like background. The red line shows the fit result. The green number is the quantity of neutrons estimated to be included in the peak, associated with the statistical error. In the pion case, the distributions associated with Λ and Σ^0 are fixed to zero.
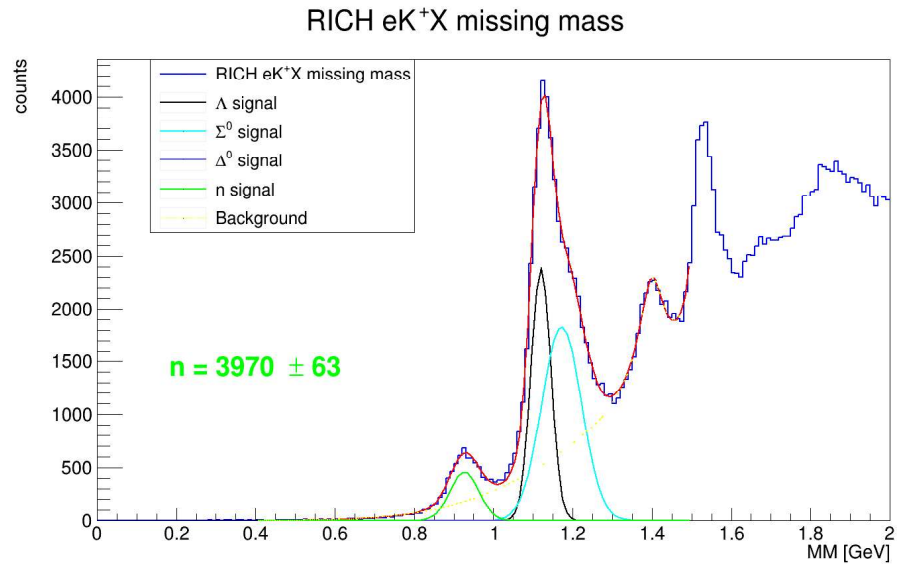
Figure 2.26: The red curve shows the fit of the missing mass plot of $eK^+ X$ states selected by the RICH using the Weibull-like background. The red line shows the fit result. The green number is the quantity of neutrons estimated to be included in the peak, associated with the statistical error. In the kaon case, the distribution associated with Δ^0 is fixed to zero.
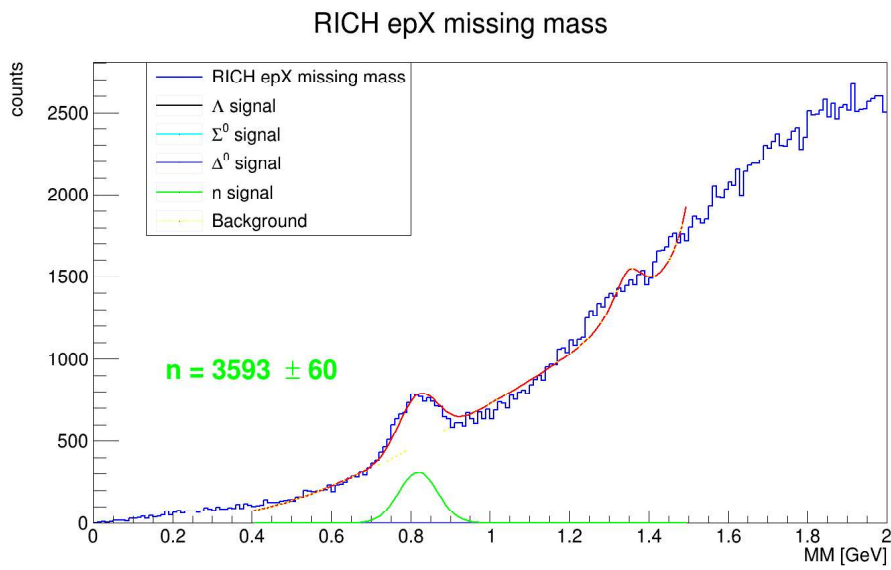
Figure 2.27: The red curve shows the fit of the missing mass plot of $e\pi X$ states selected by the RICH using the Weibull-like background. In the proton case, the neutron peak results particularly shifted with respect to the real masses 0.94 GeV because of the misidentification of pion and the wrong mass assignation. The red line shows the fit result. The green number is the quantity of neutrons estimated to be included in the peak, associated with the statistical error. In the proton case, the distributions associated with Λ, Σ^0, and Δ^0 are fixed to zero because the SIDIS background distribution is enough to describe the shape of the plot.

Figure 2.28: The red curve shows the fit of the missing mass plot of $e\pi^+ X$ states selected by the RICH and applying the cut $RQ > 0.1$. The Weibull-like background was used. The red line shows the fit result. The green number is the quantity of neutrons estimated to be included in the peak, associated with the statistical error. In the pion case, the distributions associated with Λ and Σ^0 are fixed to zero.

show the missing mass of the samples in the whole $3 \div 8 \, \text{GeV}$ momentum range without the cut on RQ, for particle identified by the RICH. The same fit was applied to the analogous plots provided by the CLAS12 PID. The number of neutrons is estimated as the integral in $(\mu - 3\sigma, \mu + 3\sigma)$ region of the Gaussian associated with the neutron peak at $0.94 \, \text{GeV}$. The reported error is the statistical uncertainty obtained as the count's square root. The missing mass plots obtained applying also the requirement $RQ > 0.1$ are shown in Figures 2.28, 2.29, and 2.30. Table 2.1 reports the number of neutrons obtained. As can be expected, with the RQ cut a slight reduction in the total statistics and a strong suppression of pion misidentifications (into kaon) are obtained. A counterintuitive phenomenon is that the pion misidentification into protons is less suppressed with the RQ cut than the one into kaons. A possible explanation is that the likelihood used in the reconstruction software assumes a variable number of photons, and weights the difference between the number of photons expected and measured. Because protons produced less Cherenov photons in the RICH momentum working range, the high mass hypothesis (proton) is favored anytime the number of detected photons is small. The studies needed to confirm this idea are beyond the aim of this analysis, which was to evaluate the purity of the kaon sample provided by the RICH.

Figure 2.29: The red curve shows the fit of the missing mass plot of eK^+X states selected by the RICH and applying the cut $RQ > 0.1$. The Weibull-like background was used. The red line shows the fit result. The green number is the quantity of neutrons estimated to be included in the peak, associated with the statistical error. In the kaon case, the distribution associated with Δ^0 is fixed to zero.
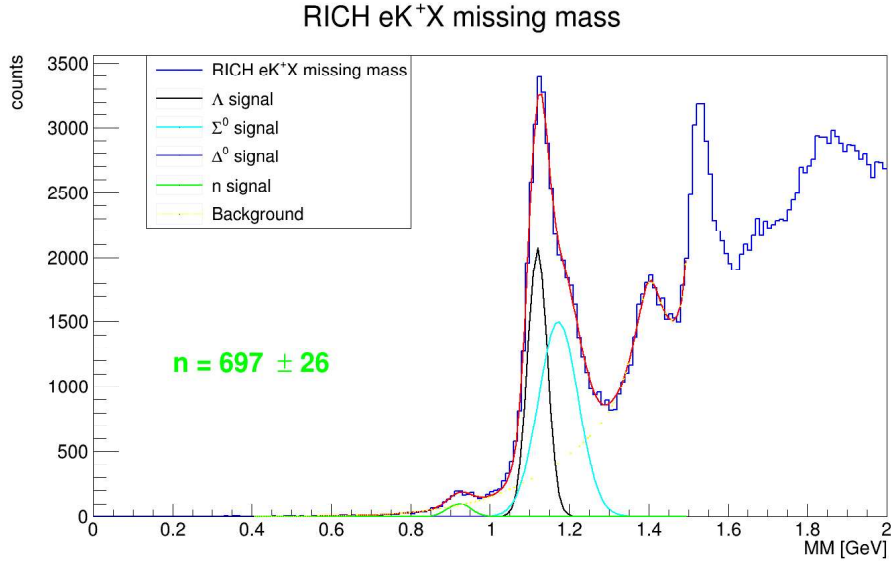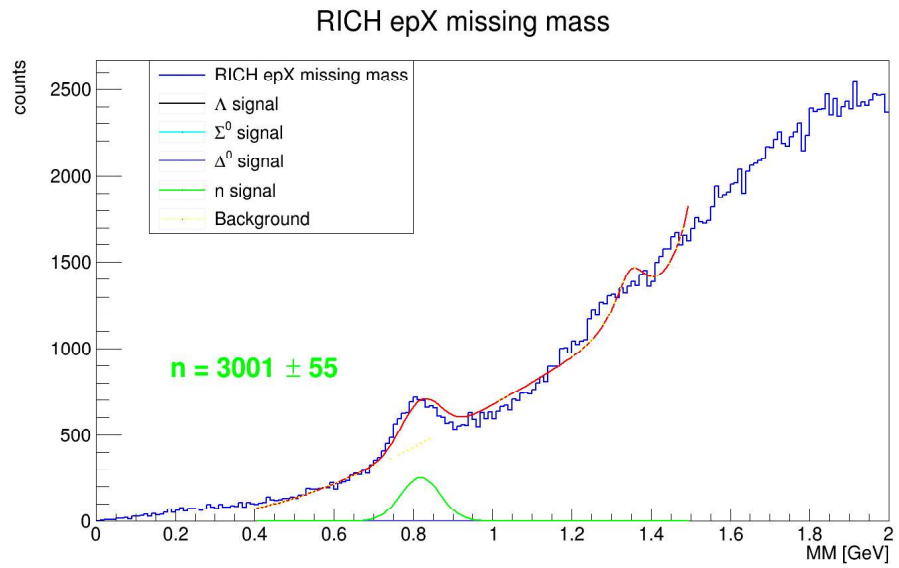
Final state	RQ cut	Number of neutrons
$e\pi^+X$	No	186943 ± 432
	Yes	171049 ± 414
eK^+X	No	3970 ± 63
	Yes	697 ± 26
epX	No	3593 ± 60
	Yes	3001 ± 55
Total	No	194506 ± 441
	Yes	174747 ± 418

Table 2.1: Recap of the number of neutrons extracted from the peak at $0.94\,\mathrm{GeV}$ in the missing mass plot.

Figure 2.30: The red curve shows the fit of the missing mass plot of $e\pi X$ states selected by the RICH and applying the cut $RQ > 0.1$. The Weibull-like background was used. In the proton case, the neutron peak results particularly shifted with respect to the real masses $0.94\,\text{GeV}$ because of the misidentification of pion and the wrong mass assignation. The red line shows the fit result. The green number is the quantity of neutrons estimated to be included in the peak, associated with the statistical error. In the proton case, the distributions associated with Λ, Σ^0, and Δ^0 are fixed to zero because the SIDIS background distribution is enough to describe the shape of the plot.

In this study, data were binned in the hadron momentum p_H inside the detector's working range: $(3, 4), (4, 5), (5, 6), (6, 8)$. An analogous study showing a possible dependence from the polar angle of the hadron was postponed after the completion of the alignment of the spherical sub-mirrors, which will extend the range up to $26°$. In this way, the photon yield can increase for particles currently on the edge of the phase space, making the identification more reliable.

2.4.3 Results

Providing a clean kaon sample

From design specification, the RICH is expected to provide a rejection factor of the pion in the kaon sample around $1 : 500$ [40]. The mean percentage of misidentification in the total momentum range without the RQ cut as derived from Table 2.1, is

$$\eta_{\pi \to K}^{RICH}(3 \, \text{GeV} < p_H < 8 \, \text{GeV}) = (2.0 \pm 0.1)\% \tag{2.10}$$

where the error is the statistical uncertainty propagated to the result. This result is not yet meeting the expected performance. By applying the RQ cut the values became

$$\eta_{\pi \to K}^{RICH}(3 \, \text{GeV} < p_H < 8 \, \text{GeV}) = (0.4 \pm 0.1)\% \tag{2.11}$$

which is close to the necessary performance to identify a clean kaon sample. The RQ cut, combined with the cuts on the minimum number of detected photons, permits to find the best trade-off between efficiency and purity, approaching the ultimate detector misidentification level of 0.2%. These selection criteria constitute a sort of preliminary quality assessment of the RICH for kaon identification. Analyzing the same events using the CLAS12 PID (without the RICH), the mean misidentification is

$$\eta_{\pi \to K}^{CLAS12}(3 \, \text{GeV} < p_H < 8 \, \text{GeV}) = (19.6 \pm 0.6)\%. \tag{2.12}$$

This huge value can be explained because the CLAS12 PID was not originally designed to distinguish efficiently high-momentum hadrons, and corroborates the decision of the CLAS collaboration to install the RICH detector. The percentage is obviously independent of the RQ cut, applying which the misidentification becomes $(18.9 \pm 0.6)\%$, as it was expected from the fact that the cut is not related to the CLAS12 PID.

The comparison of the pions misidentification as kaon provided by the RICH and the CLAS12 PID as a function of the hadron momentum is shown in Figure 2.31. It shows that the $\eta_{\pi \to K}$ for the RICH is small and substantially the same for all the momentum bins, while it grows rapidly for the CLAS12 PID.

49
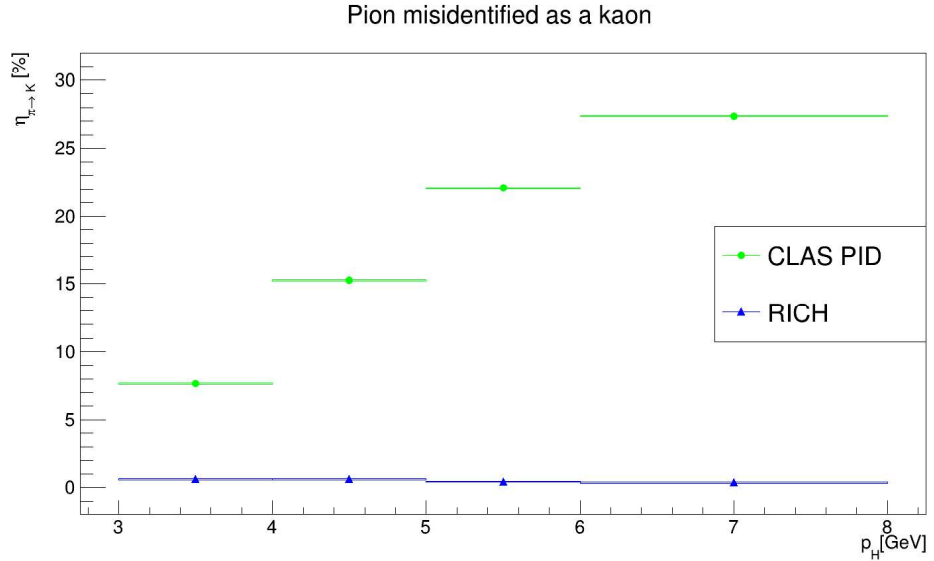
Figure 2.31: Percentage of pion misidentified as a kaon expressed as a function of the hadron momentum, applying the RQ cut. Because the error bars on the y-axis are smaller than the markers, the uncertainty was represented as a square centered on the graph point.
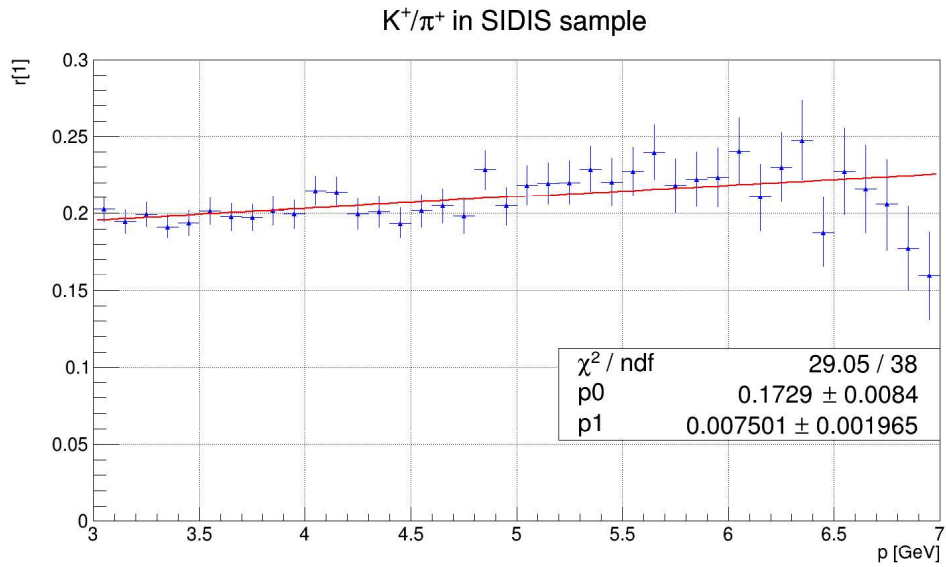
Pion contamination in kaon sample

The existence of a non-zero percentage of pions misidentified as kaons implies that there is some contamination of pions in the kaon sample. In particular, in the analyzed phase space, the pion statistic is expected to be significantly larger than the kaon statistic. The total contamination is therefore not negligible and introduces systematic effects on kaon SIDIS measurements.

To evaluate the contamination, the ratio between kaon and pion yield was studied. It is shown in Figure 2.32 as a function of the hadron momentum (the low-statistic bins were excluded). The plot was fitted using a linear function to describe the trend of the ratio as a function of the momentum. To define pion contamination $\mathcal{C}$ in the kaon sample, the probability of misidentification $\eta_{\pi \to K}(p)$ was divided by the fit result:

$$\mathcal{C} = \frac{\eta_{\pi \to K}(p)}{a_0 + p a_1} \tag{2.13}$$

where $a_{0,1}$ are the parameters and p the hadron momentum. The contamination as a function of the hadron momentum is shown in Figure 2.33. It was fitted using a linear function to quantify the dependence on momentum for the study of the systematic uncertainty due to the pion contamination in SIDIS observables, described in Chapter 3.
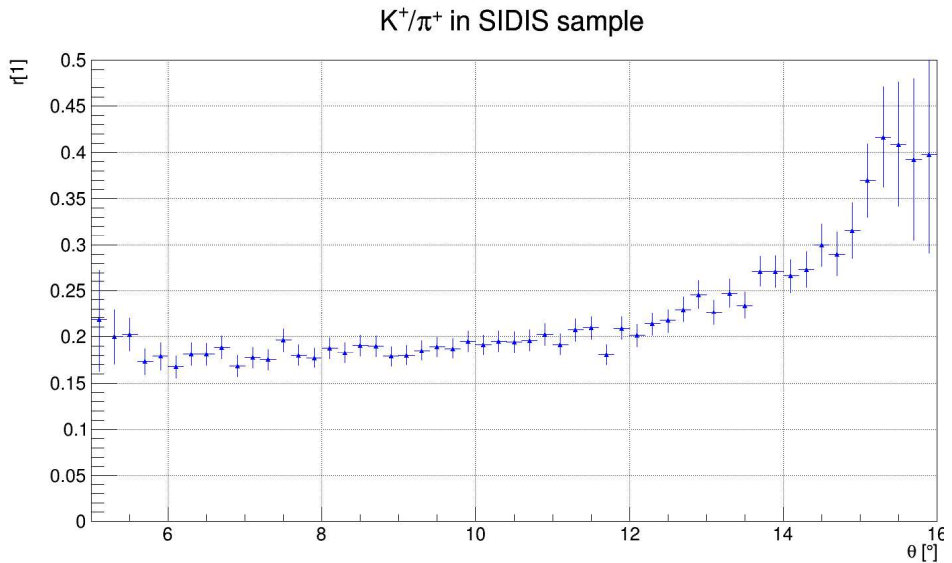
Figure 2.34 shows the ratio between kaon and pion samples as a function of the hadron polar angle (the low-statistic bins were excluded). It shows

50

Figure 2.32: Ratio between the kaon and pion distributions as a function of the hadron momentum.
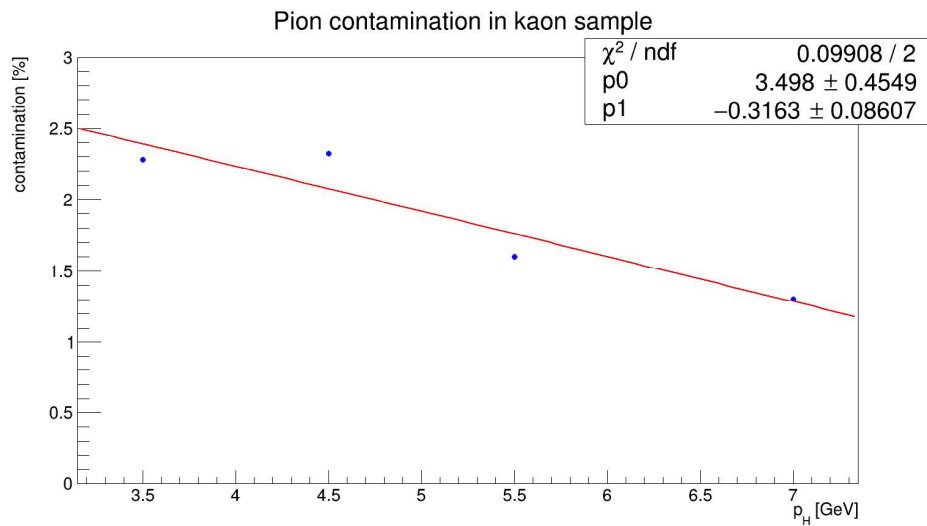
Figure 2.33: Contamination of pion in the kaon sample as a function of hadron momentum.

Figure 2.34: Ratio between the kaon and pion distributions as a function of the hadron polar angle.

a slow increase before $\theta \simeq 12°$, then the increase accelerates. Because, as shown in Figure 2.19, most of the hadrons have a polar angle between 5° and 12 degree and the kaon sample purity was not yet studied as a function of the hadron polar angle, the dependence of contamination from the polar angle was neglected in the following.
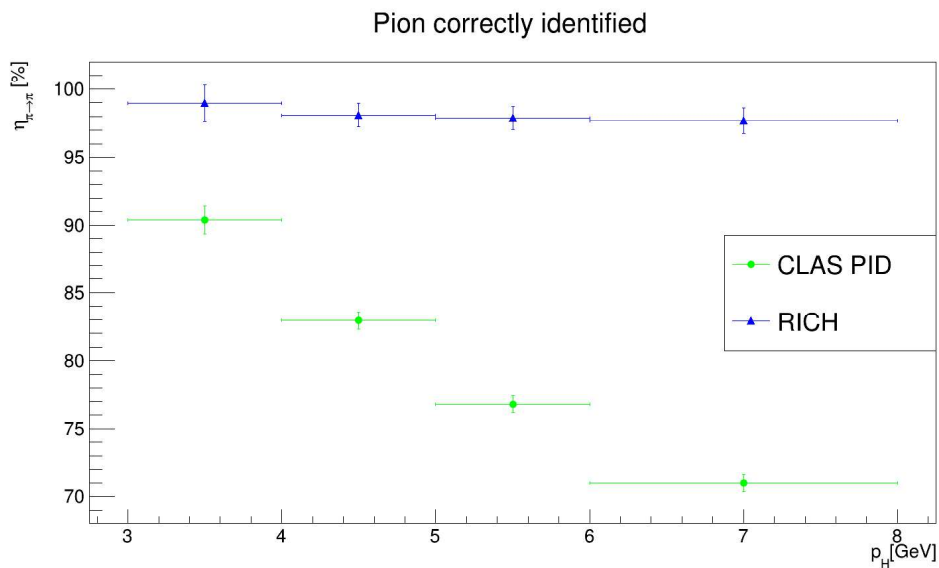
Percentage of well-identified pion

The study also provided an estimation of the percentage of pions correctly identified with respect to the number of identifications, that applying the RQ cut is

$$\eta^{RICH}_{\pi \to \pi}(3\,\text{GeV} < p_H < 8\,\text{GeV}) = (97.9 \pm 0.5)\%. \qquad (2.14)$$

The percentage of the correctly identified pions was also quantified as a function of the momentum, the comparison with CLAS12 PID performance is shown in Figure 2.35. It shows that the RICH percentage of good pion identifications slightly decreases when the momentum grows, as can be expected because the Cherenkov angle of the particles became closer. The CLAS12 PID instead quickly decreases when the momentum grows.

Summary and perspective

The Chapter described the CLAS12 RICH, including the general design of this innovative hybrid-optics detector, the assembly of the second module, and

52

Figure 2.35: Percentage of pion correctly identified over the total of pions passed through the RICH, expressed as a function of the hadron momentum. The results for RICH are obtained by applying the RQ cut.

the first study on the capability to provide a clean sample of kaons for SIDIS studies. The study presented in the last Section did not aim to perform a precise evaluation of the absolute RICH efficiency, but rather a measurement of the pion rejection factor provided by the detector. The main goal of this work is to reduce the high contamination of pions in the kaon sample identified by the CLAS12 PID (without the RICH), which originally was not designed to identify high momentum hadrons. As explained in Chapter 1, a precise PID apparatus is essential to perform SIDIS measurements, accessing the QCD dynamics with flavor sensitivity. The results show that the installation of the first RICH module provided to CLAS12 the capability to identify a clean sample of kaons, with only minimal contamination of pions. This was the first step to exploit the CLAS12 world-leading luminosity to perform high precision measurement on TMDs using kaon, complementing the ongoing studies on pion and providing new constraints to theoretical models. The next Chapter will show how the kaon sample can be used to extract a Beam-Spin Asymmetry (BSA), providing a preliminary measurement of the nucleon structure function $F_{LU}^{\sin\phi}$, which is sensitive to the TMDs with enhanced sensitivity to the strange flavor.